arXiv:0709.3150v4 [hep-lat] 10 Apr 2009

Nucleon form factors from quenched lattice QCD with domain wall fermions

Shoichi Sasaki[1,*] and Takeshi Yamazaki[2,†]

[1]*Department of Physics, The University of Tokyo, Hongo 7-3-1, Tokyo 113-0033, Japan*

[2]*Physics Department, University of Connecticut, Storrs, Connecticut 06269-3046, USA*

(Dated: April 10, 2009)

We present a quenched lattice calculation of the weak nucleon form factors: vector ($F_V(q^2)$), induced tensor ($F_T(q^2)$), axial-vector ($F_A(q^2)$) and induced pseudo-scalar ($F_P(q^2)$) form factors. Our simulations are performed on three different lattice sizes $L^3 \times T = 24^3 \times 32$, $16^3 \times 32$ and $12^3 \times 32$ with a lattice cutoff of $a^{-1} \approx 1.3$ GeV and light quark masses down to about 1/4 the strange quark mass ($m_\pi \approx 390$ MeV) using a combination of the DBW2 gauge action and domain wall fermions. The physical volume of our largest lattice is about $(3.6\ \mathrm{fm})^3$, where the finite volume effects on form factors become negligible and the lower momentum transfers ($q^2 \approx 0.1\ \mathrm{GeV}^2$) are accessible. The q^2-dependences of form factors in the low q^2 region are examined. It is found that the vector, induced tensor, axial-vector form factors are well described by the dipole form, while the induced pseudo-scalar form factor is consistent with pion-pole dominance. We obtain the ratio of axial to vector coupling $g_A/g_V = F_A(0)/F_V(0) = 1.219(38)$ and the pseudo-scalar coupling $g_P = m_\mu F_P(0.88 m_\mu^2) = 8.15(54)$, where the errors are statistical errors only. These values agree with experimental values from neutron β decay and muon capture on the proton. However, the root mean-squared radii of the vector, induced tensor and axial-vector underestimate the known experimental values by about 20 %. We also calculate the pseudo-scalar nucleon matrix element in order to verify the axial Ward-Takahashi identity in terms of the nucleon matrix elements, which may be called as the generalized Goldberger-Treiman relation.

PACS numbers: 11.15.Ha, 12.38.-t 12.38.Gc

I. INTRODUCTION

A comprehensive understanding of hadron structure, especially nucleon structure, based on quantum chromodynamics (QCD) is one of our ultimate goals in lattice QCD calculations. The latest lattice calculations of nucleon structure have been greatly developed with increasing accuracy [1]. So far, large efforts by lattice QCD simulations have been mostly devoted to studies of electro-magnetic structure of the nucleon and either unpolarized or polarized parton distributions in deep inelastic scattering [1, 2, 3, 4, 5]. However, there are only a few lattice studies to be completed for the weak nucleon form factors [6, 7], which are associated with weak probes of nucleon structure. In this paper, we present results from our intensive study of the nucleon matrix elements of the weak current in quenched lattice QCD calculations with domain wall fermions (DWFs).

Experimentally, weak processes meditated by the weak charged current like neutron beta decay $n \to p + e^- + \bar{\nu}_e$, muon capture on the proton $\mu^- + p \to \nu_\mu + n$ or quasi-elastic neutrino scattering $\bar{\nu}_\mu + p \to \mu^+ + n$ are mainly exploited for studying the weak nucleon form factors, while available information obtained from the experiment of the neutral current weak process such as semileptonic elastic scattering $\nu + p \to \nu + p$ is still limited. The weak current is known to be described by a linear combination of the vector and axial-vector currents. In general, four form factors appear in the nucleon matrix elements of the weak current. Here, for example, we consider the matrix element for neutron beta decay. In this case, the vector and axial-vector currents are given by $V_\alpha^+(x) = \bar{u}(x)\gamma_\alpha d(x)$ and $A_\alpha^+(x) = \bar{u}(x)\gamma_\alpha\gamma_5 d(x)$ and then the matrix element is expressed by

$$\begin{aligned}\langle p|V_\alpha^+(x) + A_\alpha^+(x)|n\rangle \;=\; & \bar{u}_p \left[\gamma_\alpha F_V(q^2) + \sigma_{\alpha\beta}q_\beta F_T(q^2)\right. \\ & \left. +\gamma_\alpha\gamma_5 F_A(q^2) + i q_\alpha \gamma_5 F_P(q^2)\right] u_n e^{iq\cdot x}, \end{aligned} \tag{1}$$

where $q = P_n - P_p$ is the momentum transfer between the proton (p) and neutron (n). The vector (F_V) and induced tensor (F_T) form factors are introduced for the vector matrix element, and also the axial-vector (F_A) and induced

*Electronic address: ssasaki@phys.s.u-tokyo.ac.jp

†Electronic address: yamazaki@phys.uconn.edu; Present address: Yukawa Institute for Theoretical Physics, Kyoto University, Kitashirakawa-Oiwakecho, Sakyo, Kyoto 606-8502, Japan

pseudo-scalar (F_P) form factors for the axial-vector matrix element. The vector part of weak processes are related to the nucleon's electro-magnetic form factors, which are well measured up to large momentum transfer by electron scattering [8], through an isospin rotation. Based on the conserved-vector-current hypothesis, the vector and induced tensor form factors are well understood by knowledge of the electro-magnetic structure of the nucleon.

In the axial-vector part of the weak process, the axial-vector coupling $g_A = F_A(q^2 = 0)$ is most accurately measured by neutron beta decay, where the extremely small momentum transfer is accessible due to a very small mass difference of the neutron and proton. The q^2-dependence of $F_A(q^2)$ can be determined by other processes such as quasi-elastic neutrino scattering experiments and charged pion electroproduction experiments. It has been observed that the dipole form is a good description for low and moderate momentum transfer, $q^2 < 1$ GeV^2 [9]. On the other hand, the induced pseudo-scalar form factor $F_P(q^2)$ is rather less known experimentally. The main source of information on $F_P(q^2)$ stems from muon capture. The induced pseudo-scalar coupling, $g_P = m_\mu F_P(q^2)$ evaluated at $q^2 = 0.88 m_\mu^2$, where m_μ is the muon mass, is measured by ordinary muon capture (OMC) or radiative muon capture (RMC). Although there is some discrepancy between the OMC result and the RMC result [9, 10], the new precise OMC measurement by the MuCap collaboration, which is nearly independent of μ-molecular effect, yields $g_P = 7.3 \pm 1.1$ [11]. Only a few of the other q^2 data points on $F_P(q^2)$ are measured in the low q^2 region by a single experiment of pion electroproduction [12].

Theoretically, in the axial part of such weak processes at low energies, one may consider that spontaneous chiral symmetry breaking, which is induced by the strong interaction, plays an essential role. In other words, the axial structure of the nucleon would be highly connected with the physics of chiral symmetry and its spontaneous breaking, which ensures the presence of pseudo Nambu-Goldstone particles such as the pion. This is empirically known as the partially conserved axial-vector current (PCAC) hypothesis [8], where the divergence of the axial-vector current is proportional to the pion field. Applying this idea to the axial-vector part of Eq.(1), there appears a specific relation between the residue of the pion-pole structure in $F_P(q^2)$ and the axial-vector coupling g_A known as the Goldberger-Treiman relation [13].

There was the long standing disagreement between experiment and lattice calculations about the axial-vector coupling g_A. However, the RBC Collaboration finally resolved this puzzle using quenched DWF simulations [14, 15]. DWFs are expected to provide an implementation of lattice fermions with exact chiral symmetry [16, 17, 18]. In the limit where the fifth-dimensional extent L_s is taken to infinity, DWFs preserve the axial Ward-Takahashi identity, even at a finite lattice spacing [18]. Although not sufficiently large L_s loses the virtues of DWFs, the explicit chiral symmetry breaking with moderate sizes of L_s can be attributed to a single universal "residual mass" parameter $m_{\rm res}$, acting as an additive quark mass in the axial Ward-Takahashi identity as $\partial_\alpha A_\alpha^a \approx 2(m_f + m_{\rm res})P^a$ [19, 20]. A very small value of $m_{\rm res}$, which is typically smaller than 10% of the quark mass, is always achieved at a given L_s around 10-20 with the help of improved gauge actions [20]. This fact greatly simplifies the nonperturbative determination of the renormalization of quark bilinear currents [21]. For a calculation of the axial-vector coupling g_A, the chiral symmetry is very useful because the renormalization factors of local vector and local axial-vector current operators are equal, $Z_V = Z_A$ [21]. This means that the ratio of the nucleon axial-vector and vector couplings, g_A/g_V, calculated on the lattice is not renormalized [15]. Therefore, in DWF simulations, the ambiguity in the renormalization of quark currents, which is present in other fermions such as Wilson-type fermions, is eliminated. In Ref. [15], $g_A = 1.212(27)$ in the chiral limit is obtained from quenched DWF simulations. It underestimates the experimental value of 1.2695(29) [22] by less than 5%. It has also shown that there is a significant finite volume effect between the axial-vector couplings calculated on lattices with (1.2 fm)^3 and (2.4 fm)^3 volumes. This observation strongly indicates that the axial-vector coupling is particularly sensitive to finite volume effects. Subsequently, the LHPC Collaboration has evaluated the axial-vector coupling using domain wall valence fermions with improved staggered sea quark configurations with physical volume as large as (3.5 fm)^3 and obtained $g_A = 1.226(84)$ at the physical pion mass [23]. Its value again agrees with experiment within 5%.

In this paper, we naturally extend the quenched DWF calculation for exploring the axial structure of the nucleon, namely the axial-vector form factor and the induced pseudo-scalar form factor at low q^2 as well as the electro-magnetic structure of the nucleon. Especially, to evaluate the induced pseudo-scalar coupling g_P is one of our main targets, since no intensive study has been done to determine this particular quantity in lattice QCD. Recall that the induced pseudo-scalar form factor is assumed to be dominated by a pion pole, which give rises to very rapid q^2-dependence at low q^2. The larger physical volume, where the lower momentum transfers are accessible, is required. We therefore utilize (3.6 fm)^3 volume where the smallest momentum squared ($q^2 \approx 0.1$ GeV^2) is smaller than measured pion mass squared ($m_\pi^2 > 0.15$ GeV^2). We also re-examine the finite volume effect on the axial-vector coupling using three different volumes, which include (3.6 fm)^3 together with smaller ones (1.8 fm)^3 and (2.4 fm)^3. Furthermore, we calculate the nucleon matrix element of the pseudo-scalar density $\langle p|\bar{u}\gamma_5 d|n\rangle$ to check the axial Ward-Takahashi identity in terms of the nucleon matrix elements, which may be called as the generalized Goldberger-Treiman relation [24].

Our paper is organized as follows. In Section II, we first present a brief introduction of the weak nucleon form factors and the status of experimental studies. In Section III, details of our Monte Carlo simulations and some basic results are given. We also describes the lattice method for calculating the nucleon form factors. Section IV presents

our results of the four weak form factors as well as the pseudo-scalar form factor on lattice with $(3.6\text{ fm})^3$ volume. Especially, the q^2-dependences of all measured form factors at low q^2 are discussed with great interest. At the end of this section, we discuss the consequence of the axial Ward-Takahashi identity among the axial-vector form factor, the induced pseudo-scalar form factor and the pseudo-scalar form factor. In Section V, we discuss the finite volume effects on the form factors using results from three different volumes. Meanwhile, we also check whether approximated forms of q^2-dependence of form factors, which are observed at low q^2, are still valid even in the relatively high q^2 region, up to at least $q^2 \approx 1.0\text{ GeV}^2$, apart from consideration of the finite volume effects. In Section VI, we compare our results with previous works. Finally, in Section VII, we summarize the present work and discuss future directions.

II. WEAK NUCLEON FORM FACTORS AND EXPERIMENTAL STATUS

In general, the nucleon matrix elements of the weak current are given by a linear combination of the vector and axial-vector matrix elements. Here, let us introduce the vector and axial-vector currents, which are expressed in terms of the isospin doublet of quark fields $\psi = (u, d)^T$

$$V^a_\alpha(x) = \bar{\psi}(x)\gamma_\alpha t^a \psi(x), \tag{2}$$
$$A^a_\alpha(x) = \bar{\psi}(x)\gamma_\alpha\gamma_5 t^a \psi(x), \tag{3}$$

where t^a are the $SU(2)$ flavor matrices normalized to obey $\mathrm{Tr}(t^a t^b) = \delta_{ab}$. Then, the nucleon matrix elements are given by

$$\langle N(P')|J^{\mathrm{wk}}_\alpha(x)|N(P)\rangle = \langle N(P')|V^a_\alpha(x) + A^a_\alpha(x)|N(P)\rangle \tag{4}$$
$$= \overline{u}_{_N}(P')\left(\mathcal{O}^V_\alpha(q) + \mathcal{O}^A_\alpha(q)\right) t^a u_{_N}(P) e^{iq\cdot x}, \tag{5}$$

where $q \equiv P - P'$ is the momentum transfer between the initial (P) state and the final state (P') and N represents the nucleon isospin doublet as $N = (p, n)^T$. Four form factors are needed to describe these matrix elements: the weak vector and induced tensor (weak magnetism) form factors for the vector current,

$$\mathcal{O}^V_\alpha(q) = \gamma_\alpha F_V(q^2) + \sigma_{\alpha\beta}q_\beta F_T(q^2) \tag{6}$$

and the weak axial-vector and induced pseudo-scalar form factors for the axial-vector current [54]

$$\mathcal{O}^A_\alpha(q) = \gamma_\alpha\gamma_5 F_A(q^2) + iq_\alpha\gamma_5 F_P(q^2), \tag{7}$$

which are here given in the Euclidean metric convention [55]. Thus, q^2 denoted in this paper, which stands for Euclidean four-momentum squared, corresponds to the time-like momentum squared as $q^2_M = -q^2 < 0$ in Minkowski space.

The weak matrix elements are related to the electro-magnetic matrix elements if the strange contribution is ignored under the exact iso-spin symmetry. A simple exercise in $SU(2)$ Lie algebra leads to the following relation between the vector part of the weak matrix elements of neutron beta decay and the difference of proton and neutron electro-magnetic matrix elements [8, 15]:

$$\langle p|\bar{u}\gamma_\alpha d|n\rangle = \langle p|\bar{u}\gamma_\alpha u - \bar{d}\gamma_\alpha d|p\rangle = \langle p|j^{\mathrm{em}}_\alpha|p\rangle - \langle n|j^{\mathrm{em}}_\alpha|n\rangle, \tag{8}$$

where $j^{\mathrm{em}}_\alpha = \frac{2}{3}\bar{u}\gamma_\alpha u - \frac{1}{3}\bar{d}\gamma_\alpha d$. This relation gives a connection between the weak vector and induced tensor form factors and the *iso-vector* part of electro-magnetic nucleon form factors

$$F^v_1(q^2) = F_V(q^2), \tag{9}$$
$$F^v_2(q^2) = 2M_N F_T(q^2), \tag{10}$$

where F^v_1 (F^v_2) denotes the iso-vector combination of the Dirac (Pauli) form factors of the proton and neutron, which are defined by

$$\langle N(P')|j^{\mathrm{em}}_\alpha(x)|N(P)\rangle = \overline{u}_{_N}(P')\left(\gamma_\alpha F^N_1(q^2) + \sigma_{\alpha\beta}\frac{q_\beta}{2M_N}F^N_2(q^2)\right) u_{_N}(P), \tag{11}$$

where M_N denotes the nucleon mass, which is defined as the average of neutron and proton masses, and N represents p (proton) or n (neutron). Experimental data from elastic electron-nucleon scattering is usually presented in terms of the electric $G_E(q^2)$ and magnetic $G_M(q^2)$ Sachs form factors which are related to the Dirac and Pauli form factors [8, 26]

$$G^N_E(q^2) = F^N_1(q^2) - \frac{q^2}{4M^2_N}F^N_2(q^2), \tag{12}$$
$$G^N_M(q^2) = F^N_1(q^2) + F^N_2(q^2). \tag{13}$$

Their normalization at $q^2 = 0$ are given by the proton (neutron) charge and magnetic moment [22]:

$$\begin{array}{ll} \text{Proton:} & G_E^p(0) = 1,\ G_M^p(0) = \mu_p = +2.792847351(28), \\ \text{Neutron:} & G_E^n(0) = 0,\ G_M^n(0) = \mu_n = -1.91304273(45). \end{array} \tag{14}$$

Therefore, one finds $F_V(0) = G_E^p(0) - G_E^n(0) = 1$ and $2M_N F_T(0) = G_M^p(0) - G_M^n(0) - 1 = 3.70589$. As for the q^2-dependence of the form factors, it is experimentally known that the standard dipole parametrization $G_D(q^2) = \Lambda^2/(\Lambda^2 + q^2)$ with $\Lambda = 0.84$ GeV (or $\Lambda^2 = 0.71$ GeV^2) describes well the magnetic form factors of both the proton and neutron and also the electric form factor of the proton, at least, in the low q^2 region [26]. Here, the current interesting issues of the q^2-dependence of the electro-magnetic form factors at higher q^2 are beyond the scope of this paper. Recent reviews on the experimental situation can be found in Ref. [26]. The slopes of the form factors at $q^2 = 0$ determine mean-squared radii, which can be related to dipole masses as $\langle r_i^2 \rangle = 12/M_i^2$ ($i = E$ or M) in the dipole form $G_i(q^2) = G_i(0)/(1 + q^2/M_i^2)$. The experimental values of the electric root mean-squared (rms) radius for the proton and the magnetic rms radii of the proton and neutron are compiled in Table I. These rms radii are all equal within errors and are in agreement with the empirical dipole parameter Λ. On the other hand, the slope of the neutron electric form factor $G_E^n(q^2)$ is determined with high precision from double-polarization measurements of neutron knock-out from a polarized ^{2}H or ^{3}He target, while only a small deviation from zero is observed for $G_E^n(q^2)$ at low q^2 [26]. Combined with all four of the electric charge and magnetization radii of the proton and neutron, we finally evaluate the rms radii for the weak vector form factor and induced tensor form factor as $\sqrt{\langle (r_V)^2 \rangle} = 0.797(4)$ fm and $\sqrt{\langle (r_T)^2 \rangle} = 0.879(18)$ fm, which correspond to the dipole masses, $M_V = 0.857(8)$ GeV and $M_T = 0.778(23)$ GeV. See Appendix A for details.

The axial-vector form factor at zero momentum transfer, namely the axial-vector coupling $g_A = F_A(0)$, is precisely determined by measurements of the beta asymmetry in neutron decay. The value of $g_A = 1.2695(29)$ is quoted in the 2006 PDG [22]. Nevertheless, kinematics of neutron beta decay are quite limited due to a very small mass difference of the proton and neutron. Other experimental methods are utilized for determination of the q^2-dependence of $F_A(q^2)$. For this purpose, there are basically two types of experiment, namely quasi-elastic neutrino scattering and charged pion electroproduction experiments. The former suffers from severe experimental uncertainties concerning the incident neutrino flux and the background subtraction of elastic events, while model-dependent analysis is somewhat inevitable for the latter [9]. Both methods reported that the dipole form $F_A(q^2) = F_A(0)/(1 + q^2/M_A^2)$ is a good description for low and moderate momentum transfer, $q^2 < 1$ GeV^2. The resulting world average of the dipole mass parameter M_A is quoted as $M_A = 1.026(21)$ GeV from neutrino scattering or $M_A = 1.069(16)$ GeV from pion electroproduction in Ref. [9]. As for a small discrepancy between two averages, it has been argued that within heavy-baryon chiral perturbation theory (HBChPT) the finite pion mass correction of -0.055 GeV to the latter value may resolve this discrepancy [9]. Therefore, one can translate the axial dipole mass into the axial rms radius of $\sqrt{\langle (r_A)^2 \rangle} = 0.67(1)$ fm, which is consistently obtained from quasi-elastic neutrino scattering experiments and charged pion electroproduction experiments [9].

On the other hand, the induced pseudo-scalar form factor $F_P(q^2)$ is less well-known experimentally [10]. The main source of information on $F_P(q^2)$ stems from ordinary muon capture (OMC) on the proton, $\mu^- + p \to \nu_\mu + n$. One measures the induced pseudo-scalar coupling $g_P = m_\mu F_P(q_0^2)$ at the specific momentum transfer for the muon capture by the proton at rest as $q_0^2 = 0.88 m_\mu^2$. The induced pseudo-scalar coupling g_P is also measured in radiative muon capture (RMC), $\mu^- + p \to \gamma + \nu_\mu + n$. Before 2006, the Saclay OMC experiment, which was the most recent OMC experiment at that time, reported $(g_P^{\rm OMC})_{\rm Saclay,original} = 8.7 \pm 1.9$ [28]. Combining with the older OMC experiments including bubble chamber measurements, the world average for OMC is obtained as $(g_P^{\rm OMC})_{\rm old\ Ave} = 8.79 \pm 1.92$, which is given in Refs. [9] and [28]. Surprisingly, this value is close to the theoretically predicted value by HBChPT, $g_P^{\rm ChPT} = 8.26 \pm 0.16$ [9]. However, the novel RMC experiment at TRIUMF [29, 30] is puzzling: their measured value of $g_P^{\rm RMC} = 12.4 \pm 1.0$ is quite higher than the theoretical value as is the OMC value as $g_P^{\rm RMC} \approx 1.4 g_P^{\rm OMC}$. This disagreement is reduced by reanalysis with the updated μ^+ lifetime [10]. Then, the updated result of the Saclay OMC experiment yields $(g_P^{\rm OMC})_{\rm Saclay,updated} = 10.6 \pm 2.7$. Accordingly, the weighted world average for OMC, $(g_P^{\rm OMC})_{\rm updated\ Ave.} = 10.5 \pm 1.8$ given in Ref. [10], is shifted away from the theoretical expected value, while the updated average value is in agreement with the RMC result within its error. Indeed, there is a caveat that the ortho-para transition rate in μ-molecular Hydrogen, to which either OMC and RMC results are very sensitive, is poorly known due to mutually inconsistent results among two experiments [28, 31] and theory [32]. Comprehensive reviews of a history of g_P have been given in Refs.[9] and [10].

Recently, a new OMC experiment has been done by the MuCap Collaboration [11]. The MuCap result is nearly independent of μ-molecular effects in contrast with the previous OMC experiments and the RMC experiment. After the electro-weak radiative corrections, which were underestimated in the old literature, are correctly taken into account [33], the new precise OMC measurement yields

$$g_P^{\rm MuCap} = 7.3 \pm 1.1. \tag{15}$$

Including the new MuCap result and taking into account the electro-weak radiative corrections, the new world average of the OMC results becomes $(g_P^{\rm OMC})_{\rm newAve} = 8.7 \pm 1.0$ [33]. As for other q^2 data of $F_P(q^2)$, only a few data points are measured in the low q^2 region by a single experiment of pion electroproduction at threshold [12]. These data are summarized in Table II. Three data points from pion electroproduction at threshold are well fitted by the pion-pole dominance form, $F_P(q^2) = 2M_N F_A(q^2)/(q^2 + m_\pi^2)$ [35], which is also consistent with the value determined by the new OMC result at $q^2 = 0.88 m_\mu^2$. Therefore, the pion-pole dominance is confirmed, more or less, through pion electroproduction [12].

III. SIMULATION DETAILS

We work in the quenched approximation and use domain wall fermions (DWFs) to compute the nucleon matrix elements of the weak current. We generate ensembles of the quenched QCD configuration with the renormalization group improved, DBW2 (doubly blocked Wilson in two-dimensional parameter space) gauge action [36, 37] at $\beta = 6/g^2 = 0.87$ ($a^{-1} \approx 1.3$ GeV), where the residual chiral symmetry breaking of domain wall fermions is significantly improved with a moderate size of the fifth-dimension L_s such as $L_s = 16$ [20]. Indeed, the residual quark mass for $L_s = 16$ is measured as small as $m_{\rm res} \sim 5 \times 10^{-4}$ in lattice units [20], which is safely negligible compared with the input quark masses in our simulations, $0.02 \le m_f \le 0.08$. We work with relatively coarse lattice spacing, $a \approx 0.15$ fm [56], which is determined from the ρ meson mass [20].

To study finite volume effects, numerical simulations are performed on three different lattice sizes $L^3 \times T = 24^3 \times 32$, $16^3 \times 32$ and $12^3 \times 32$. The spatial extents in our study correspond to $La \simeq 3.6$, 2.4 and 1.8 fm. Quark propagators are generated for four bare masses $m_f = 0.02$, 0.04, 0.06 and 0.08 for $L = 24$ and three bare masses $m_f = 0.04$, 0.06 and 0.08 for $L = 16$ and 12, using DWFs with $L_s = 16$ and $M_5 = 1.8$. Details of our simulations are summarized in Table III. In Table IV, some basic physics results are compiled from Ref. [20].

The pseudo-scalar meson (pion) masses computed in these calculations are summarized in Table V. All fitted values are obtained from the covariant single cosh fit. It is clear that there is no visible finite-volume effect on the pion mass. Measured values for $L = 16$ are in good agreement with the values found in Ref. [15], where point-to-box quark propagators are used with the mostly same gauge ensembles, while the point-to-gauss-smeared quark propagators are utilized in the present study. Our simulated values of the pion mass range from 0.39 GeV to 0.76 GeV.

A. Nucleon spectra and Dispersion relation

In order to compute nucleon masses or matrix elements, we define the nucleon (proton) operator as

$$\chi^S(t, \mathbf{p}) = \sum_{\mathbf{x}} e^{-i\mathbf{p}\cdot\mathbf{x}} \varepsilon_{abc} [u_a^T(\mathbf{y}_1, t) C\gamma_5 d_b(\mathbf{y}_2, t)] u_c(\mathbf{y}_3, t) \times \phi(\mathbf{y}_1 - \mathbf{x})\phi(\mathbf{y}_2 - \mathbf{x})\phi(\mathbf{y}_3 - \mathbf{x}), \tag{16}$$

where abc and ud have usual meanings as color and flavor indices. C is the charge conjugation matrix defined as $C = \gamma_t\gamma_y$ and the superscript T denotes transpose. The superscript S of the nucleon operator χ specifies the smearing for the quark propagators. In this study, we use two types of source: local source as $\phi(\mathbf{y}_i - \mathbf{x}) = \delta(\mathbf{y}_i - \mathbf{x})$ and Gaussian smeared source. Here we take $\mathbf{y}_1 = \mathbf{y}_2 = \mathbf{y}_3 = \mathbf{0}$ in our calculation. As for the Gaussian smeared source, we apply the gauge-invariant Gaussian smearing [41, 42] with $N = 30$, $\omega = 4.35$. Details of our choice of smearing parameters are described in Ref. [43].

We construct two types of the two-point function for the proton. One interpolating operator at the source location is constructed from Gaussian smeared quark fields, while the other interpolating operator at the sink location is either constructed from local quark fields (denoted LG) or Gaussian smeared ones (denoted GG):

$$C_{SG}(t - t_{\rm src}, q) = \frac{1}{4}{\rm Tr}\left\{\mathcal{P}_+ \langle \chi^S(t, \mathbf{q})\overline{\chi^G}(t_{\rm src}, -\mathbf{q})\right\}, \tag{17}$$

with $S = L$ or G. The projection operator $\mathcal{P}_+ = \frac{1+\gamma_t}{2}$ can eliminate contributions from the opposite-parity state for $q^2 = 0$ [44, 45]. It is rather expensive to make the Gaussian smeared interpolating operator projected onto a specific finite momentum at the source location ($t_{\rm src}$). However, it is sufficient to project only the sink operator onto the desired momentum by virtue of momentum conservation. Thus, the quark fields at the source location are not projected onto any specific momentum in this calculation. For the momentum at the sink location ($t_{\rm sink}$), we take all possible permutations of the three-momentum $\mathbf{q}$ including both positive and negative directions.

Nucleon masses and energies are computed by using the LG correlators with the five lowest momenta: $(0,0,0)$, $(1,0,0)$, $(1,1,0)$, $(1,1,1)$ and $(2,0,0)$ in units of $2\pi/L$. All fitted values, which are obtained from the conventional

single exponential fit, for each volume are summarized in Table V. Next, we examine the dispersion relation of the nucleon state in our simulations. The purpose of this examination is two fold: 1) Our analysis should be restricted to the lower momenta that do not suffer from large $\mathcal{O}(a^2)$ errors. 2) The evaluation of the squared four-momentum transfer q^2 requires precise knowledge of the nucleon energies with finite momentum. The later point can be achieved by an estimation of the energy $E(\mathbf{p})$ with the help of the dispersion relation and the measured nucleon rest mass M_N that can be most precisely measured.

For $m_f = 0.04$ the measured values of the nucleon energy, which are obtained from $L = 24$ (open circles), $L = 16$ (open squares) and $L = 12$ (open diamonds), are compared with the relativistic dispersion relation

$$E(\mathbf{p}) = \sqrt{\mathbf{p}^2 + M_N^2} \tag{18}$$

in Fig. 1 with either the naive discrete (continuum-like) momentum $p_i = \frac{2\pi}{L} n_i$ or the lattice discrete momentum $p_i = \sin[\frac{2\pi}{L} n_i]$ $(n_i = 0, 1, 2, \cdots, (L-1))$ for $\mathbf{p} = (p_x, p_y, p_z)$. We observe that the measured energies $E(\mathbf{p})$ are consistent with the estimated values from the relativistic dispersion formula for continuum-like momenta (dashed-dotted curve) and lattice momenta (dashed curve) in the range of our admitted momentum except for the largest momentum on the lattice with $L = 12$ as shown in Fig. 1 . The difference between either choice of the discrete momentum is mostly comparable to the statistical errors, while differences increase at the larger momentum. To restrict ourselves to low q^2 region ($q^2 < 1$ GeV^2), we do not use the two largest momenta on the lattice with $L = 12$ for the proceeding analysis. Therefore, it is not a concern to choose what type of the discrete momentum in the dispersion relation in our current calculation. We simply choose the continuum-like momentum throughout this paper and then evaluate the values of the squared four-momentum transfer q^2 with the measured rest mass M_N and the continuum dispersion relation (18).

B. Three point correlation functions

As discussed in the previous section, under the exact iso-spin symmetry ($m_u = m_d$), the $SU(2)$ current algebra leads to the following relations [8, 15]

$$\langle p|V_\alpha^+|n\rangle = 2\langle p|V_\alpha^3|p\rangle, \tag{19}$$
$$\langle p|A_\alpha^+|n\rangle = 2\langle p|A_\alpha^3|p\rangle, \tag{20}$$

where $V_\alpha^3 = \frac{1}{2}(\bar{u}\gamma_\alpha u - \bar{d}\gamma_\alpha d)$ and $A_\alpha^3 = \frac{1}{2}(\bar{u}\gamma_\alpha\gamma_5 u - \bar{d}\gamma_\alpha\gamma_5 d)$. Thus, we may calculate the weak transition matrix elements by the iso-vector proton matrix elements.

First of all, we define the finite-momentum three-point functions for the relevant components of either the local vector current ($\mathcal{J}_\alpha^V(x) = \bar{u}(x)\gamma_\alpha u(x) - \bar{d}(x)\gamma_\alpha d(x)$) or the local axial-vector current ($\mathcal{J}_\alpha^A(x) = \bar{u}(x)\gamma_\alpha\gamma_5 u(x) - \bar{d}(x)\gamma_\alpha\gamma_5 d(x)$) with the proton interpolating operator χ:

$$\langle \chi(t', \mathbf{p}')\mathcal{J}_\alpha^\Gamma(t, \mathbf{q})\overline{\chi}(0, -\mathbf{p})\rangle = \mathcal{G}_\alpha^\Gamma(p, p') \times f(t, t', E(\mathbf{p}), E(\mathbf{p}')) + \cdots, \tag{21}$$

where the initial and final proton states carry fixed momenta $\mathbf{p}$ and $\mathbf{p}'$ respectively and then the current operator has a three-dimensional momentum transfer $\mathbf{q} = \mathbf{p} - \mathbf{p}'$. Here, Dirac indices have been suppressed. The ellipsis denotes excited state contributions which can be ignored in the case of $t' - t \gg 1$ and $t \gg 1$. We separate the correlation function into two parts: $\mathcal{G}_\alpha^\Gamma(p, p')$ which is defined as

$$\mathcal{G}_\alpha^\Gamma(p, p') = (-i\gamma \cdot p' + M_N)\mathcal{O}_\alpha^\Gamma(q)(-i\gamma \cdot p + M_N), \tag{22}$$

where $\mathcal{O}_\alpha^\Gamma(q)$ corresponds to either Eq.(6) or Eq.(7), and the factor $f(t, t', E(\mathbf{p}), E(\mathbf{p}'))$ which collects all the kinematical factors, normalization of states, and time dependence of the correlation function. The trace of $\mathcal{G}_\alpha^\Gamma(p, p')$ with some appropriate projection operator $\mathcal{P}$ for specific combinations of Γ and α yields some linear combination of form factors in each Γ channel. On the other hand, all time dependences of the factor $f(t, t', E(\mathbf{p}), E(\mathbf{p}'))$ can be eliminated by the appropriate ratio of three- and two-point functions [2, 3]

$$\mathcal{R}(t) = \frac{C_{\Gamma,\alpha}^{\mathcal{P}}(t, \mathbf{p}', \mathbf{p})}{C^{GG}(t_{\rm sink} - t_{\rm src}, \mathbf{p}')} \left[\frac{C^{LG}(t_{\rm sink} - t, \mathbf{p})C^{GG}(t - t_{\rm src}, \mathbf{p}')C^{LG}(t_{\rm sink} - t_{\rm src}, \mathbf{p}')}{C^{LG}(t_{\rm sink} - t, \mathbf{p}')C^{GG}(t - t_{\rm src}, \mathbf{p})C^{LG}(t_{\rm sink} - t_{\rm src}, \mathbf{p})}\right]^{\frac{1}{2}}, \tag{23}$$

where

$$C_{\Gamma,\alpha}^{\mathcal{P}}(t, q) = \frac{1}{4}\mathrm{Tr}\left\{\mathcal{P}\langle\chi^G(t_{\rm sink}, \mathbf{p}')\mathcal{J}_\alpha^\Gamma(t, \mathbf{q})\overline{\chi^G}(t_{\rm src}, -\mathbf{p})\rangle\right\}, \tag{24}$$

which are calculated by the sequential source method described in Ref. [15]:

In this study, we consider only the case at the rest frame of the final state ($\mathbf{p}' = \mathbf{0}$), which leads to $\mathbf{q} = \mathbf{p}$. Therefore, the squared four-momentum transfer is given by $q^2 = 2M_N(E(\mathbf{q}) - M_N)$. Nucleon energy $E(\mathbf{q})$ is simply abbreviated as E, hereafter. In this kinematics, $\mathcal{G}^\Gamma_\alpha(p, p')$ is represented by a simple notation as $\mathcal{G}^\Gamma_\alpha(q)$. Then, the ratio (23) gives the asymptotic form as a function of the current-operator insertion time t,

$$\mathcal{R}(t) \to \frac{1}{4}\mathrm{Tr}\{\mathcal{P}\mathcal{G}^\Gamma_\alpha(q)\} \times \frac{1}{\sqrt{2M_N^2 E(E+M_N)}} \tag{25}$$

in the limit when the Euclidean time separation between all operators is large, $t_{\rm sink} \gg t \gg t_{\rm src}$ with fixed $t_{\rm src}$ and $t_{\rm sink}$.

We choose particular combinations of the projection operator $\mathcal{P}$ and the current operator $\mathcal{J}^\Gamma_\alpha$ ($\Gamma = V$ or A). We consider two types of the projection operator, $\mathcal{P}^t = \mathcal{P}_+\gamma_t$ and $\mathcal{P}^z_5 = \mathcal{P}_+\gamma_5\gamma_z$ in this study. The latter projection operator implies that the z-direction is chosen as the polarized direction. We then obtain some linear combination of desired form factors from the projected correlation functions,

$$\frac{1}{4}\mathrm{Tr}\left\{\mathcal{P}^t\mathcal{G}^V_t(q)\right\} = M_N(E+M_N)\left[F_V(q^2) - (E-M_N)F_T(q^2)\right], \tag{26}$$

$$\frac{1}{4}\mathrm{Tr}\left\{\mathcal{P}^z_5\mathcal{G}^V_i(q)\right\} = -i\varepsilon_{ijz}q_j M_N\left[F_V(q^2) + 2M_N F_T(q^2)\right], \tag{27}$$

for the vector currents $\mathcal{J}^V_t$ and $\mathcal{J}^V_i$ ($i = x, y, z$). Similarly, we get

$$\frac{1}{4}\mathrm{Tr}\left\{\mathcal{P}^z_5\mathcal{G}^A_i(q)\right\} = M_N(E+M_N)\left[F_A(q^2)\delta_{iz} - \frac{q_i q_z}{E+M_N}F_P(q^2)\right], \tag{28}$$

for the axial-vector current $\mathcal{J}^A_i$ ($i = x, y, z$). In this calculation, we use at most the four non-zero three-momentum transfer $\mathbf{q} = \frac{2\pi}{L}\mathbf{n}$ ($\mathbf{n}^2 = 1,\ 2,\ 3,\ 4$). All possible permutations of the lattice momentum including both positive and negative directions are properly taken into account. All three-point correlation functions are calculated with a source-sink separation of 10 in lattice units, which is the same in the previous DWF calculation of the axial-vector coupling g_A [15]. For $L = 24$, we calculate three-point correlation functions with three different sequential sources generated with source-sink locations, $[t_{\rm src}, t_{\rm sink}] = [0, 10]$, $[10, 20]$, and $[20, 30]$ on a given gauge configuration [57], while only a single sequential source with $[t_{\rm src}, t_{\rm sink}] = [0, 10]$ is utilized for $L = 12$ and $L = 16$ calculations.

In Fig. 2, we plot the dimensionless projected correlators

$$\Lambda^V_0 = \frac{\frac{1}{4}\mathrm{Tr}\{\mathcal{P}^t\mathcal{G}^V_t(q)\}}{M_N(E+M_N)}, \tag{29}$$

$$\Lambda^V_T = -\frac{1}{2}\left(\frac{\frac{1}{4}\mathrm{Tr}\{\mathcal{P}^z_5\mathcal{G}^V_x(q)\}}{iq_y M_N} - \frac{\frac{1}{4}\mathrm{Tr}\{\mathcal{P}^z_5\mathcal{G}^V_y(q)\}}{iq_x M_N}\right), \tag{30}$$

as a function of the current insertion time slice t for $m_f = 0.04$ on the largest volume ($L = 24$) as typical examples. Good plateaus for all squared three-momentum transfer are observed in the middle region between the source and sink points. The quoted errors are estimated by a single elimination jack-knife method. The lines plotted in each figure represent the average value (solid lines) and their one standard deviations (dashed lines) in the time-slice range $3 \le t \le 7$.

Similarly, Fig. 3 shows Λ^A_L and Λ^A_T for the axial vector current, which are defined by

$$\Lambda^A_L = \frac{\frac{1}{4}\mathrm{Tr}\{\mathcal{P}^z_5\mathcal{G}^A_z(q)\}}{M_N(E+M_N)}, \tag{31}$$

$$\Lambda^A_T = -\frac{1}{2}\left(\frac{\frac{1}{4}\mathrm{Tr}\{\mathcal{P}^z_5\mathcal{G}^A_x(q)\}}{q_z q_x} + \frac{\frac{1}{4}\mathrm{Tr}\{\mathcal{P}^z_5\mathcal{G}^A_y(q)\}}{q_z q_y}\right). \tag{32}$$

It is worth noting that in the axial-vector channel the z-direction is chosen as the polarized direction in this study. Therefore, the longitudinal momentum (q_z) dependence explicitly appears in Eq. (28). This fact provides two kinematical constraints on determination of the three-point functions in our calculation. First, there are two types of kinematics, $q_z \neq 0$ and $q_z = 0$ in the longitudinal component ($i = z$) of Eq. (28), except for the case of $\mathbf{n}^2 = 3$ where q_z is always non-zero. Secondly, the transverse components ($i = x$ or y) of Eq. (28) are prevented from vanishing by the kinematics only if $\mathbf{n}^2 = 2$ and 3, where two components of the momentum including the polarized direction

(z-direction) are non-zero. These are the reasons why $\Lambda_L^A(q_z=0)$ and $\Lambda_L^A(q_z\neq 0)$ are separately plotted in Fig. (3) and results of $\Lambda_L^A(q_z=0)$ at $\mathbf{n}^2=3$ and Λ_T^A at $\mathbf{n}^2=1$, 4 are missing there.

Finally, we recall that the lattice local operators $\mathcal{J}_\alpha^\Gamma(x)$ ($\Gamma=V$ or A), which are represented as the quark bilinear currents, receive finite renormalizations relative to their continuum counterparts. Thus the renormalized form factors require some independent estimation of Z_Γ, the renormalization of the quark bilinear currents, $[\mathcal{J}_\alpha^\Gamma]^{\rm ren}=Z_\Gamma[\mathcal{J}_\alpha^\Gamma]^{\rm lattice}$. As mentioned previously, good chiral properties of DWFs ensure that the lattice renormalizations of the local currents are equal, $Z_V=Z_A$, up to terms of order $\mathcal{O}(a^2)$ in the chiral limit and neglecting explicit chiral symmetry breaking due to the moderate size of the fifth-dimensional extent L_s [21]. In this paper, we evaluate Z_V at each quark mass from the inverse of $F_V(0)$ that should be unity in the continuum under the exact $SU(2)$ iso-spin symmetry and multiply four weak form factors by this renormalization factor Z_V to estimate the renormalized form factors in the chiral limit.

C. Vector coupling g_V and axial-vector coupling g_A

At zero three-momentum transfer $|\mathbf{q}|=0$, only Λ_0^V and Λ_L^A are calculable. Then, these directly yield the values of $(g_V)^{\rm lattice}$ and $(g_A)^{\rm lattice}$ respectively. Our results of $(g_V)^{\rm lattice}$, $(g_A)^{\rm lattice}$ and their ratio $(g_A)^{\rm ren}=(g_A/g_V)^{\rm lattice}$ obtained in this calculation are summarized in Table VI, where old results for $L=8$ and $L=16$ calculated in Ref. [15] are also tabulated. In Fig. 4, we show the ratios of the axial to the vector coupling $(g_A/g_V)^{\rm lattice}$ calculated for three different volumes as functions of pion mass squared. Clearly, the finite volume effect on $(g_A/g_V)^{\rm lattice}$ can be observed. The larger volume results exhibit milder quark mass dependence, while the smallest volume results show a slow downward tendency toward the chiral limit away from the experimental point. Therefore, for the largest volume results, we simply adopt a linear extrapolation with respect to the pion mass squared to take the chiral limit. We obtain the axial-vector coupling $g_A^{\rm ren}=1.219(38)$ at the physical point ($m_\pi=0.14$ GeV).

We next examine more details of the finite volume effect on the vector and axial-vector couplings separately. Combined results from three different spatial sizes, $La\approx 1.8$ fm, 2.4 fm and 3.6 fm together with old results from $La\approx 1.2$ fm, we plot $(g_V)^{\rm lattice}$ and $(g_A)^{\rm lattice}$ against the spatial lattice size in the physical unit in Fig. 5. The quoted errors in the figure represent only the statistical errors, which are obtained by a single elimination jack-knife method. The left (right) figure is for lighter (heavier) pion mass. The axial-vector coupling $(g_A)^{\rm lattice}$ shows the significant spatial-size dependence, while we do not see any serious finite volume effect on the vector coupling $(g_V)^{\rm lattice}$. This indicates that the observed finite volume effect in Fig. 4 stems from that of $(g_A)^{\rm lattice}$. Clearly, it is observed that $(g_A)^{\rm lattice}$ decreases monotonically with decreasing spatial size L. Therefore, we simply utilize the power-law formula to estimate the infinite volume limit of the axial-vector coupling as

$$g_A^{\rm lattice}(L)=g_A^{\rm lattice}(\infty)+bL^{-n} \tag{33}$$

with the power three ($n=3$). Horizontal lines in figures represent the values in the infinite volume limit and their one standard deviations. The values obtained from the largest volume, $(3.6\text{ fm})^3$, are quite close to the values in the infinite volume limit. At a glance, the spatial size over 2.5 fm is large enough to accurately calculate the axial-vector coupling, at least within the range of our admitted quark mass.

We finally quote

$$g_A^{\rm ren}=1.219\pm 0.038(\text{stat})\pm 0.024(\text{norm})\pm 0.002(\text{volume}), \tag{34}$$

where the second error is evaluated from a 2 % error stemming from $Z_V\neq Z_A$, which was observed previously [15] and the third error is estimated from a difference between the extrapolated value in the infinite volume limit and the largest volume result at $m_f=0.04$.

IV. RESULTS OF NUCLEON FORM FACTORS ON A $(3.6\text{ fm})^3$ VOLUME

In this section, we focus on the results obtained from lattice size $24^3\times 32$, which corresponds to physical volume, $V\approx(3.6\text{fm})^3$. The lower momentum is admitted by the larger spatial extent L. Therefore, we can make the shorter extrapolation with respect to q^2 toward the forward limit, $q^2=0$, for nucleon form factors, $F_T(q^2)$ and $F_P(q^2)$, of which values at $q^2=0$ cannot be accessible directly due to the kinematical constraint as described before. We also discuss the finite size effect on the nucleon form factors, which may be sensitive to the nucleon "wave function" or the nucleon "size" squeezed due to the finite spatial extent of lattice volume. In the previous section, the spatial lattice-size dependence of the axial-vector coupling shows that spatial lattice size $La\approx 3.6$ fm is large enough to avoid significant finite volume effect on g_A.

A. Vector channel

In the case if spatial momentum transfer **q** is non-zero, all three-point correlation functions defined in Eqs.(26) and (27) are calculable. Two independent form factors $F_V(q^2)$ and $F_T(q^2)$ are obtained by

$$F_V(q^2) = \frac{2M_N}{E+M_N}\Lambda_0^V + \frac{E-M_N}{E+M_N}\Lambda_T^V, \tag{35}$$

$$F_T(q^2) = \frac{1}{E+M_N}\left(-\Lambda_0^V + \Lambda_T^V\right) \tag{36}$$

at finite q^2.

1. *Dirac form factor $F_V(q^2)$*

First, we show quark mass dependence of the Dirac form factor $F_V(q^2)$. In Fig. 6, we plot the normalized $F_V(q^2)$ by $F_V(0)$ as a function of four-momentum squared q^2. Different symbols represent the values obtained from different quark masses m_f. There is no large m_f-dependence, while it seems that the smaller quark mass makes the q^2-dependence steeper. The Dirac form factor is supposed to be the dipole form at low q^2:

$$F_V(q^2) = \frac{F_V(0)}{(1+q^2/M_V^2)^2}, \tag{37}$$

where M_V denotes the dipole mass. A dashed curve in Fig. 6 corresponds to the dipole form with the empirical value of the dipole mass $M_V = 0.857(8)$ GeV, which is evaluated from the electric charge and magnetization radii of the proton and neutron as described in Appendix A.

In order to see how our measured $F_V(q^2)$ has an expected dipole form, we define the following quantity only at nonzero momentum:

$$M_V^{\rm eff}(q^2) = \sqrt{\frac{q^2\sqrt{F_V(q^2)}}{\sqrt{F_V(0)}-\sqrt{F_V(q^2)}}}, \tag{38}$$

which should provide q^2 independent plateau if the q^2-dependence of $F_V(q^2)$ ensures the dipole form. We call this quantity the effective dipole mass hereafter. In Fig. 7, we show the effective dipole-mass plot for the Dirac form factor at $m_f = 0.02$ as a typical example. Horizontal solid and dashed lines represent the fitted dipole mass obtained from a correlated fit to $F_V(q^2)$ using the dipole form (37) and its one standard deviation. The dotted lines shows the empirical dipole mass, $M_V = 0.857(8)$ GeV. Clearly, there is no appreciable q^2-dependence of the effective dipole mass within statistical errors. Even at the highest $q^2 \approx 0.44$ GeV^2, the fitted dipole mass agrees with the value of the effective dipole mass. Therefore, we conclude that the dipole form describes well the q^2-dependence of our measured Dirac form factor $F_V(q^2)$. This observation is consistent with previous studies [2, 4].

Fig. 8 shows the quark-mass dependence of the fitted dipole mass. As seen from this figure, the quark-mass dependence is rather mild and then there is no appreciable curvature as a function of the pion mass squared. Therefore, we simply adopt a linear extrapolation with respect to the pion mass squared to evaluate the value of the dipole mass of $F_V(q^2)$ in the chiral limit. Diamond symbols in Fig. 8 are extrapolated values for the chiral limit ($m_\pi = 0$) and the physical point ($m_\pi = 0.14$ GeV) and the solid line represents the fitted line. Our measured dipole masses of the Dirac form factor are much larger than the experimental value. Here we recall that the root mean-squared (rms) radii can be determined with the corresponding dipole mass as $\sqrt{\langle r_V^2\rangle} = \sqrt{12}/M_V$. The larger dipole mass M_V means that the spatial size of the nucleon in our simulations is smaller than the physical one. This may be attributed to the missing large "pion-cloud" contribution since it is well known that the mean-squared radius $\langle r_V^2\rangle$ receives a large pion loop correction, which leads to a logarithmic divergence in the chiral limit in heavy baryon chiral perturbation theory [46]. Indeed, the present calculation is still far from the chiral regime: our smallest pion mass is around 0.39 GeV which is comparable to the lightest pion mass in the most recent lattice study of nucleon electro-magnetic form factors [4]. Although the expected chiral behavior is not guaranteed in the quenched approximation, in the present study the estimation of systematic errors stemming from quenching and a long chiral extrapolation is beyond the scope of this paper. Rather we would like to see how large volume can be fitted for studying the structure of the nucleon, namely, the nucleon form factors without significant finite volume effect. Studies of the finite size effect on the nucleon form factors using results obtained from three different lattice sizes will be presented in the next section.

2. Pauli form factor $F_T(q^2)$

In Fig. 9, we show the Pauli form factor $F_2(q^2) = 2M_N F_T(q^2)$ as a function of four-momentum squared q^2. The form factor plotted here is scaled by the renormalization factor $Z_V = 1/F_V(0)$ to get the renormalized one, $F_2^{\rm ren}(q^2) = Z_V F_2(q^2)$. In contrast with Fig. 6, large m_f-dependence is observed. As well as the Dirac form factor, the Pauli form factor is phenomenologically supposed to be the dipole form at low q^2:

$$F_2^{\rm ren}(q^2) = \frac{F_2^{\rm ren}(0)}{(1+q^2/M_T^2)^2}, \tag{39}$$

where the value of $F_2^{\rm ren}(q^2)$ at $q^2 = 0$ is associated with the difference of the proton and neutron magnetic moments, $\mu_p - \mu_n = 1 + F_2^{\rm ren}(0)$. This dipole form is commonly adopted as a fitting form of the q^2 extrapolation to evaluate $F_2^{\rm ren}(0)$ in published works [2, 4]. We also plot the dipole form with the empirical value of the Pauli dipole mass $M_T = 0.778(23)$ GeV and the experimental values of μ_p and μ_n in the same figure. Our results of $F_2^{\rm ren}(q^2)$ gradually approach this dipole form as m_f decreases. Indeed, data points for $m_f = 0.02$ in the range of our calculated q^2 follow the experimental curve within the statistical error. However, if we apply the dipole form to the data, our obtained values of $F_2^{\rm ren}(0)$ from dipole fits are somewhat underestimated in comparison with the experimental value $\mu_p - \mu_n - 1 = 3.70589$ as shown in Fig. 10.

In contrast to the Dirac form factor, we cannot try the effective dipole mass plot for a justification of the applied dipole form, since we do not have data of $F_2^{\rm ren}(0)$ without the q^2 extrapolation. Instead, we consider an independent observation for the difference of μ_p and μ_n, which can be derived from the forward limit of the ratio of the magnetic form factor $G_M(q^2)$ and the electric form factor $G_E(q^2)$. The ratio is calculated by a different combination of Λ_0^V and Λ_T^V [43] as

$$\frac{G_M(q^2)}{G_E(q^2)} = \frac{G_M^{\rm ren}(q^2)}{G_E^{\rm ren}(q^2)} = \frac{\Lambda_T^V}{\Lambda_0^V}. \tag{40}$$

Experimentally, it is known that this ratio shows no q^2-dependence at low q^2 since both form factors are well fitted by the dipole form with the comparable dipole masses [8, 26]. Therefore, this ratio may yield the constant value identified to $\mu_p - \mu_n = G_M^{\rm ren}(0)$. Indeed, in our calculation, the proposed ratio (40) exhibits no appreciable q^2-dependence in the range of our calculated q^2. We may use a simple linear fitting form with respect to four-momentum squared q^2 for an alternative evaluation of the value $\mu_p - \mu_n$. Fig. 10 shows that two determinations to evaluate $\mu_p - \mu_n - 1$ are consistent with each other.

In Fig. 11, we plot values of $\mu_p - \mu_n$, which are evaluated by two determinations, $1 + F_2^{\rm ren}(0)$ and $G_M(0)/G_E(0)$, as a function of pion mass squared m_π^2. As described above, both determinations fairly agree with each other. Although the values measured at two heaviest points are consistent with the experimental one, a strong m_π^2 dependence appears near the chiral limit and then the extrapolated value tends to somewhat underestimate the experimental data. Here, we simply adopt a linear fit with respect to m_π^2 regardless of the fact that a slight downward curvature is observed in Fig. 11.

We also extrapolate the Pauli dipole mass M_T to the chiral limit in Fig. 12. Again, we use a simple linear fitting form for the chiral extrapolation. The value obtained at the physical point is about a 20% overestimation in comparison with the experimental one, the same as in the case of the Dirac dipole mass. This indicates that corresponding rms radii are somewhat smaller than the actual nucleon size. Finally, all fitted results with the dipole form for both form factors and their extrapolated values to the chiral limit are summarized in Table VII.

B. Axial-vector channel

In the axial-vector channel, two independent form factors $F_A(q^2)$ and $F_P(q^2)$ can be evaluated separately by

$$F_A(q^2) = \Lambda_L^A(q_z = 0), \tag{41}$$
$$F_P(q^2) = \Lambda_T^A / M_N \tag{42}$$

at finite q^2. It should be reminded that $\Lambda_L^A(q_z = 0)$ at $\mathbf{n}^2 = 3$ and Λ_T^A at $\mathbf{n}^2 = 1, 4$ are not obtained directly from corresponding three-point functions due to the kinematics as described in the previous section. However, instead, we can evaluate them by using a relation

$$\Lambda_L^A(q_z \neq 0) = \Lambda_L^A(q_z = 0) - \frac{q_z^2}{M_N(E + M_N)}\Lambda_T^A, \tag{43}$$

where $\Lambda_L^A(q_z \neq 0)$ are always calculable at finite q^2.

1. Axial-vector form factor $F_A(q^2)$

Fig. 13 shows quark mass dependence of the axial-vector form factor $F_A(q^2)$. The vertical axis is normalized by $F_A(0)$ and the horizontal axis denotes the four-momentum squared q^2 in physical units. Different symbols represent the values obtained from different quark mass m_f. The axial-vector form factor is phenomenologically fitted with the dipole form, at least at low q^2, as well as the Dirac and Pauli form factors [9]:

$$F_A(q^2) = \frac{F_A(0)}{(1 + q^2/M_A^2)^2}, \tag{44}$$

where M_A denotes the axial dipole mass. A dashed curve in Fig. 13 shows the dipole form with an experimental value of the axial dipole mass $M_A = 1.026(21)$ GeV [9]. There is a similarity here in comparison with Fig. 6. No large m_f-dependence is observed. Even at the smallest quark mass $m_f = 0.02$, where the corresponding pion mass is less than 400 MeV, our observed $F_A(q^2)$ is far from the experimental curve. Indeed, the axial-vector form factor $F_A(q^2)$ is flatter than the experimental one, similar to what we observe in $F_V(q^2)$ and $F_2(q^2) = 2M_N F_T(q^2)$. This again indicates that the nucleon size in coordinate space shrinks away. The similar observation is reported in Ref. [7].

Next, to see how the dipole form is fitted to our measured $F_A(q^2)$, we show the effective dipole mass plot, which was defined similarly to Eq.(38). Fig. 14 is plotted for $m_f = 0.02$ as a typical example. We also include the fitted M_A, which is obtained from a correlated fit to $F_A(q^2)$ using the dipole form (44), with its one standard deviation as solid and dashed horizontal lines. All momentum points except the third one, which deviates from the fitted value by about 2σ, are located within the horizontal lines. Here, we remark that the third momentum point of $F_A(q^2)$ at $m_f = 0.02$ in Fig. 13 is slightly dropped from the values measured at other quark masses. We then stress that the case of $m_f = 0.02$ is the worst example. Indeed, it is found that the effective dipole mass plot for heavier m_f are quite consistent with the fitted values in all q^2 range that we measured. From this observation, we conclude that the q^2-dependence of our measured $F_A(q^2)$ can be well described by the dipole form (44) in the range of our utilized q^2, ($q^2 \leq 0.44$ GeV^2). This is quite consistent with the phenomenological knowledge on the q^2-dependence of $F_A(q^2)$.

We show the quark-mass dependence of the fitted axial dipole mass as a function of the pion mass squared in Fig. 15. All measured values are listed in Table VIII. We find that the quark-mass dependence is somewhat milder than the dipole masses for the Dirac and Pauli form factors. Clearly, there is no appreciable curvature as a function of the pion mass squared. As before, we simply adopt a linear extrapolation for the axial dipole mass M_A toward the chiral limit. The extrapolated values (diamond symbols) overestimate the experimental one marked by the asterisk in Fig. 15.

As pointed out before, our observed "size" of the nucleon in coordinate space is much smaller than the experimental one. We will see that there is no significant finite volume effect, which may cause the "size" of the nucleon to be squeezed on the lattice with (3.6 fm)^3 volume. Thus, this observed "squeezing", which is evident from the broadening of the form factors, may be attributed to the missing contribution of the "pion-cloud" surrounding the nucleon outside of the chiral regime. Interestingly, however, the ratio of the axial dipole mass to the Dirac dipole mass is in very good agreement with the experiment. In Fig 16, we show the ratio M_A/M_V together with the ratio M_T/M_V as a function of the pion mass squared. The quark mass dependence of both ratios is found to be very mild in our observed range of m_π^2. All measured values of M_A/M_V and M_T/M_V, which are listed in Table IX, are fairly comparable to their respective experimental values. We obtain $M_A/M_V = 1.285(73)$ and $M_T/M_V = 0.869(57)$ at the physical point by using a simple linear extrapolation.

2. Induced pseudo-scalar form factor $F_P(q^2)$

First, we show the quark-mass dependence of the induced pseudo-scalar form factor $F_P(q^2)$ in Fig. 17. In contrast to the axial-vector form factor $F_A(q^2)$, significant m_f-dependence is observed especially in the lower q^2 region ($q^2 < 0.3$ GeV^2). This might be associated with the pion-pole contribution to $F_P(q^2)$, which is expected theoretically. Indeed, the partially conserved axial-vector current (PCAC) hypothesis and pion-pole dominance (PPD) predict that the induced pseudo-scalar form factor approximately behaves like

$$F_P^{\rm PPD}(q^2) = \frac{2M_N F_A^{\rm ren}(q^2)}{q^2 + m_\pi^2}, \tag{45}$$

which becomes exact in the chiral limit where the pion is massless ($m_\pi = 0$) [8, 35]. The single pion electroproduction experiment also supports the PPD form [12]. Here, to see how the pion-pole behavior is preserved in $F_P(q^2)$ measured

in the quenched calculation, we consider the following ratio

$$\alpha_{\rm PPD} = \frac{F_P^{\rm ren}(q^2)}{F_P^{\rm PPD}(q^2)}, \tag{46}$$

which is inspired by the above PCAC prediction. If the measured $F_P(q^2)$ has exactly the same form described in Eq.(45), the ratio $\alpha_{\rm PPD}$ yields the value of unity in the entire q^2 region.

In Fig. 18, we plot the above defined ratio $\alpha_{\rm PPD}$ as a function of four-momentum squared q^2. This figure shows two important features. The significant quark-mass dependence observed in Fig. 17 almost disappears as expected. Furthermore, there is no appreciable q^2-dependence in $\alpha_{\rm PPD}$. Clearly, four different q^2 points of $\alpha_{\rm PPD}$ reveal q^2 independent plateau within the statistical errors. We simply take the weighted average of $\alpha_{\rm PPD}$ within four measured q^2 points, then plot them against the pion mass squared. As shown in Fig. 19, the average values of $\alpha_{\rm PPD}$ gradually approach unity as the pion mass decreases. However, a simple linear extrapolation of $\alpha_{\rm PPD}$ yields a value slightly smaller than 1 even in the chiral limit. As a result, measured $F_P^{\rm ren}(q^2)$ is quit well described by the PPD form with a multiplicative (quenching) factor $\alpha_{\rm PPD} < 1$.

$$F_P^{\rm ren}(q^2) \approx \alpha_{\rm PPD} \times F_P^{\rm PPD}(q^2). \tag{47}$$

The validity of the PPD form is also tested by the other analysis. Following the analysis done in the previous study of the q^2-dependence of $F_P(q^2)$ [7], we apply the monopole fit to the ratio $F_P(q^2)/F_A(q^2)$. The satisfactory consistency between the fitted monopole mass and the measured pion mass is observed in our DWF calculation [58], while both quenched and unquenched Wilson simulations fail to exhibit the correct pion-pole structure of $F_P(q^2)$ [7].

Next, we evaluate the induced pseudo-scalar coupling, which is defined by $(g_P)^{\rm ren} = m_\mu F_P^{\rm ren}(0.88m_\mu^2)$ where m_μ is the muon rest mass and $F_P^{\rm ren}(q^2) = F_P(q^2)/F_V(0)$. The specific momentum transfer for muon capture ($q^2 = 0.88m_\mu^2$) is still far from our lowest momentum transfer ($q^2 \approx 0.1$ GeV^2) so that the determination of $(g_P)^{\rm ren}$ requires the q^2 extrapolation of $F_P^{\rm ren}(q^2)$. We have already learned that the q^2-dependence of measured $F_P^{\rm ren}(q^2)$ is well described by the PPD-like form (47) in the low q^2 region. Therefore, the induced pseudo-scalar coupling can be evaluated by

$$(g_P)^{\rm ren} = \frac{2m_\mu M_N}{m_\pi^2 + 0.88m_\mu^2} \times \alpha_{\rm PPD} F_A^{\rm ren}(0.88m_\mu^2), \tag{48}$$

where $F_A^{\rm ren}(0.88m_\mu^2)$ is precisely determined through the q^2 interpolation with the help of the dipole form and very accurate data $F_A^{\rm ren}(0)$. The pion mass in Eq.(48) is simply replaced by its physical value in order to subtract the dominant source of the large m_f-dependence. In Fig. 20, we plot the resulting value of $(g_P)^{\rm ren}$ (square symbols) as a function of the pion mass squared. All measured values are listed in Table VIII. Although there still remains the explicit dependence of the quark mass, the simple linear extrapolation yields $(g_P)^{\rm ren} = 8.15 \pm 0.54$ at the physical point ($m_\pi = 0.14$ GeV).

Here, the observed m_f-dependence stems from that of measured M_N, since both $\alpha_{\rm PPD}$ and $F_A^{\rm ren}(q^2)$ have a very mild quark mass dependence. To diminish the explicit m_f-dependence, we may evaluate the dimensionless prefactor in Eq.(48) with the experimental values of $m_\mu = 105.7$ MeV, $m_\pi = 139.6$ MeV and $M_N = 938.9$ MeV instead of using measured values. We then obtain a more simple form as $(g_P)^{\rm ren} = 6.77 \times \alpha_{\rm PPD} F_A^{\rm ren}(0.88m_\mu^2)$, which is similar to the known phenomenological form for g_P beside the quenching factor $\alpha_{\rm PPD}$ [10]. Indeed, evaluated values using this simple formula have no appreciable m_f dependence as shown in Fig. 20. After the linear extrapolation, we obtained $(g_P)^{\rm ren} = 7.31 \pm 0.39$ at the physical point. Two determinations provide consistent results within their statistical errors. Of course, the latter determination is rather phenomenological, then we prefer to quote the former value for our final result. We finally quote

$$(g_P)^{\rm ren} = 8.15 \pm 0.54({\rm stat}) \pm 0.16({\rm norm}), \tag{49}$$

where the second error is an estimate of a 2% error stemming from $Z_V \neq Z_A$, the same as in the axial-vector coupling g_A.

This value is to be compared with the most recent experimental value $g_P^{\rm exp} = 7.3 \pm 1.1$ from the MuCap experiment [11], where the obtained value of $g_P^{\rm exp}$ is nearly independent of μ-molecular effects. We also quote the prediction of chiral perturbation theory, $g_P^{\rm ChPT} = 8.26 \pm 0.23$ and the new world average of experimental values, $g_P^{\rm exp} = 8.7 \pm 1.0$ [33] obtained from ordinary muon capture including the new MuCap result.

Phenomenologically, the residue of the pion pole in the induced pseudo-scalar form factor is related to the pion-nucleon coupling $g_{\pi NN}$ [35]. The induced pseudo-scalar form factor should be expressed as

$$F_P^{\rm ren}(q^2) \simeq \frac{2F_\pi g_{\pi NN}}{q^2 + m_\pi^2} \tag{50}$$

near the pion pole ($q^2 \approx -m_\pi^2$) [8, 35] with the renormalized pion decay constant F_π, which is defined as $Z_A\langle 0|\partial_\alpha A_\alpha^a(x)|\pi_b(q)\rangle = m_\pi^2 F_\pi \delta_{ab} e^{iq\cdot x}$ [59]. This parameterization provides a way to evaluate the pion-nucleon coupling $g_{\pi NN}$ from the measured induced pseudo-scalar form factor as follows:

$$g_{\pi NN} = \lim_{q^2 \to -m_\pi^2} (q^2 + m_\pi^2) \frac{F_P^{\rm ren}(q^2)}{2F_\pi} \tag{51}$$

$$= \frac{\alpha_{\rm PPD}}{F_\pi} \times M_N F_A^{\rm ren}(-m_\pi^2), \tag{52}$$

where the second equality follows from our observed form (47) on $F_P^{\rm ren}(q^2)$. The value of $F_A^{\rm ren}(-m_\pi^2)$ is evaluated by the dipole form with measured $F_A^{\rm ren}(0)$, M_A and m_π. We then obtain

$$g_{\pi NN} = 10.4 \pm 1.0(\text{stat}) \tag{53}$$

at the physical point. Our obtained value is about 20% smaller that a recent estimation $g_{\pi NN} = 13.32 \pm 0.09$ ($g_{\pi NN}^2/4\pi = 14.11 \pm 0.20$) obtained from forward πN scattering data [47].

C. Pseudo-scalar channel

1. *Pseudo-scalar form factor $G_P(q^2)$*

In this study, we also calculate the pseudo-scalar nucleon matrix element

$$\langle N(P')|P^a(x)|N(P)\rangle = \overline{u}_{_N}(P')\mathcal{O}^P(q)t^a u_{_N}(P)e^{iq\cdot x}, \tag{54}$$

which is associated with the axial-vector matrix element through the axial Ward-Takahashi identity. Here, $P^a(x)$ is a local pseudo-scalar density, $P^a(x) \equiv \bar{\psi}(x)\gamma_5 t^a \psi(x)$. The pseudo-scalar matrix element can be described only by a single form factor, which is called the pseudo-scalar form factor $G_P(q^2)$:

$$\mathcal{O}^P(q) = \gamma_5 G_P(q^2). \tag{55}$$

To extract the form factor, therefore, we simply calculate the following trace of $\mathcal{G}^P(q)$, which represents the spinor structure of the corresponding three-point function, with the projection operator $\mathcal{P}_5^z$:

$$\frac{1}{4}\mathrm{Tr}\left\{\mathcal{P}_5^z \mathcal{G}^P(q)\right\} = iq_z M_N G_P(q^2), \tag{56}$$

where the definition of $\mathcal{G}^P(q)$ is given by Eqs. (21) and (22) with the local current $\mathcal{J}_5^P(x) = \bar{u}(x)\gamma_5 u(x) - \bar{d}(x)\gamma_5 d(x)$. It is apparent that non-zero three-momentum $\mathbf{q} \neq \mathbf{0}$ is required to access the pseudo-scalar form factor. In other words, $G_P(q^2)$ in the vicinity of $q^2 = 0$ cannot be evaluated without q^2 extrapolation.

In Fig. 21, we show the m_f-dependence of the pseudo-scalar form factor $G_P(q^2)$. Significant m_f-dependence is observed in the lower q^2 region, similar to the induced pseudo-scalar form factor $F_P(q^2)$. We will discuss the q^2-dependence on $G_P(q^2)$ from the viewpoint of pion-pole dominance later.

2. *Test for the axial Ward-Takahashi identity*

First, we address the question whether our domain wall fermion (DWF) calculations of nucleon form factors satisfy the axial Ward-Takahashi identity. A similar study has been recently done with the Wilson fermions in both quenched and unquenched simulations [7].

In the limit where the fifth-dimensional extent L_s is taken to infinity, domain wall fermions preserve the axial Ward-Takahashi identity at nonzero lattice spacing [18]. The axial Ward-Takahashi identity for the DWF with $SU(2)$ iso-spin symmetry is

$$\partial_\mu \mathcal{A}_\mu^a(x) = 2m_f J_5^a(x) + 2J_{5q}^a(x), \tag{57}$$

where $\mathcal{A}_\mu^a$ is the partially-conserved axial-vector current, which is point split and requires sums over the extra fifth dimension of the DWF, J_5^a is a usual bilinear pseudo-scalar density corresponding to P^a, and J_{5q}^a is a similar pseudo-scalar density defined at the midpoint of the fifth dimension. The "midpoint" term J_{5q}^a is responsible for the explicit

chiral symmetry breaking due to the finiteness of the fifth-dimension [18]. With moderate L_s, this effect can be described by the so-called residual mass term $m_{\rm res}$. Then, Eq.(57) can be approximately represented by

$$\partial_\alpha \mathcal{A}^a_\alpha(x) \approx 2(m_f + m_{\rm res})P^a(x). \tag{58}$$

This residual mass $m_{\rm res}$ is determined by $\langle 0|J^a_{5q}|\pi\rangle/\langle 0|J^a_5|\pi\rangle$. The value of $m_{\rm res}$ is known to be small in this calculation. (See Table IV.)

For a practical reason, we did not use the conserved axial-vector current for evaluating the nucleon axial matrix element in this study. Instead, we use the local axial-vector current $A^a_\mu = \bar\psi\gamma_\mu\gamma_5 t^a\psi$, which may be related to the conserved axial-vector current as $\mathcal{A}_\mu = Z_A A_\mu + \mathcal{O}(a^2, m_f a^2)$. It is worth mentioning that $Z_V = Z_A$ is satisfied up to small discretization errors of $\mathcal{O}(a^2)$ in the chiral limit [15]. We also did not measure the nucleon matrix element of J^a_{5q}, therefore we cannot fully check the axial Ward-Takahashi identity (AWT) in terms of the nucleon matrix element in this paper. Instead, we test the following ratio, which may have no apparent q^2-dependence.

$$\alpha_{\rm AWT} = \frac{2M_N F_A^{\rm ren}(q^2) - q^2 F_P^{\rm ren}(q^2)}{2m_f G_P(q^2)}, \tag{59}$$

This ratio (59) is associated with the following identity [60]:

$$Z_A\langle N|\partial_\alpha A^a_\alpha(x)|N\rangle = 2m_{\rm AWT}\langle N|P^a(x)|N\rangle, \tag{60}$$

where $m_{\rm AWT} \equiv \alpha_{\rm AWT} m_f$, which is expected to be comparable to $m_f + m_{\rm res}$ up to terms of order $\mathcal{O}(a^2, m_f a^2)$.

As shown in Fig.22, indeed, there is no appreciable q^2-dependence in the ratio $\alpha_{\rm AWT}$ for each m_f. Four different q^2 points of $\alpha_{\rm AWT}$ reveal a q^2-independent plateau within the statistical errors. We evaluate the weighted average of $\alpha_{\rm AWT}$ by using all four measured q^2 points. The obtained values of $\alpha_{\rm AWT}$ are tabulated in Table X. Deviation from unity is getting large as m_f decreases [61]. This indicates that $\alpha_{\rm AWT}$ may possess a $1/m_f$ term, which is induced by the presence of the additive mass shift in the axial Ward-Takahashi identity such as $m_{\rm res}$. To see this point clearly, we plot the modified ratio as $m_f(\alpha_{\rm AWT} - 1)$, which can be interpreted as the difference between $m_{\rm AWT}$ and m_f. Fig. 23 shows modified ratios as functions of four-momentum squared q^2 for all four values of m_f. There is again no visible q^2 dependence. Moreover, all m_f results are consistent with each other within statistical errors. $m_{\rm shift} \equiv m_{\rm AWT} - m_f$, which is given by taking the weighted average of four q^2 points in Fig. 23, corresponds to the relative amplitude of $\langle N|J^a_{5q}|N\rangle$ to the usual pseudo-scalar matrix element $\langle N|J^a_5|N\rangle$. More precisely, $m_{\rm shift}$ is expressed by

$$m_{\rm shift} = \frac{\langle N|J^a_{5q}|N\rangle}{\langle N|J^a_5|N\rangle} + \mathcal{O}(a^2, m_f a^2). \tag{61}$$

Therefore, supposing that $\langle N|J^a_{5q}|N\rangle/\langle N|J^a_5|N\rangle \approx \langle 0|J^a_{5q}|\pi\rangle/\langle 0|J^a_5|\pi\rangle$, we expect $m_{\rm shift} \approx m_{\rm res}$ besides $\mathcal{O}(a^2, m_f a^2)$ corrections. We plot $m_{\rm shift}$ against the pion mass squared in Fig. 24. The mild m_f-dependence allows us to take a linear extrapolation for $m_{\rm shift}$ to the chiral limit. At $m_f = 0$, we obtain $m_{\rm shift} = 0.0073(12)$, which is about one order of magnitude larger than $m_{\rm res} = 5.69(26) \times 10^{-4}$ [20] contrary to our naive expectation. A few % level $\mathcal{O}(a^2)$ correction, which is observed in the difference between Z_V and Z_A cannot account for this discrepancy. To resolve it, it is necessary to calculate the relative amplitude of $\langle N|J^a_{5q}|N\rangle$ to the usual pseudo-scalar matrix element $\langle N|J^a_5|N\rangle$ directly. We plan to study $\langle N|J^a_{5q}|N\rangle$ as well as $\langle N|\mathcal{A}^a_\alpha|N\rangle$ with the conserved axial-vector current $\mathcal{A}_\alpha$ in our extended work [48].

3. Test for the pion-pole dominance on $G_P(q^2)$

According to the pion-pole dominance of $F_P(q^2)$, we may expect that the pion-pole dominance holds even in $G_P(q^2)$. As described in Appendix B, a naive pion-pole dominance hypothesis predicts the ratio of the pseudo-scalar form factor and induced pseudo-scalar form factor, will not depend on q^2 at low q^2 but will exhibit a constant value, related to the low energy constant B_0. Indeed, this is not the case. In Fig. 25, we show the ratio of our measured $G_P(q^2)$ and $F_P(q^2)$ as a function of momentum squared q^2. There is a linear-like q^2 dependence, which strengthens as the quark mass decreases. However, as we will describe below, we confirm that the pion-pole dominance on $G_P(q^2)$ still remains valid in our calculation.

What we have observed in the previous subsection can be interpreted as a consequence of the axial Ward-Takahashi identity among three nucleon form factors:

$$2M_N F_A^{\rm ren}(q^2) - q^2 F_P^{\rm ren}(q^2) \approx 2m_{\rm AWT} G_P(q^2). \tag{62}$$

Combined with this relation and the important observation of pion-pole dominance in $F_P(q^2)$ (Eq.(47)), one may expect that the q^2-dependence of $G_P(q^2)$ is mostly described by the pion-pole dominance form with a slight modification, which corresponds to an extra q^2-dependence caused by the fact that $\alpha_{\rm PPD} \neq 1$:

$$G_P(q^2) \approx \frac{1+(1-\alpha_{\rm PPD})\frac{q^2}{m_\pi^2}}{\alpha_{\rm AWT}} \times G_P^{\rm PPD}(q^2), \tag{63}$$

where the naive pion-pole dominance form [49] is defined as

$$2m_f G_P^{\rm PPD}(q^2) = 2M_N F_A^{\rm ren}(q^2)\frac{m_\pi^2}{q^2+m_\pi^2}. \tag{64}$$

This residual q^2-dependence due to $\alpha_{\rm PPD} \neq 1$ is supposed to be responsible for the q^2-dependence in the ratio of our measured $G_P(q^2)$ and $F_P^{\rm ren}(q^2)$

$$\frac{G_P(q^2)}{F_P^{\rm ren}(q^2)} \approx \frac{1+(1-\alpha_{\rm PPD})\frac{q^2}{m_\pi^2}}{\alpha_{\rm PPD}\alpha_{\rm AWT}}\frac{G_P^{\rm PPD}(q^2)}{F_P^{\rm PPD}(q^2)} = \Delta_{\rm PPD}(q^2)\frac{m_\pi^2}{2m_{\rm AWT}}, \tag{65}$$

where $\Delta_{\rm PPD}(q^2) \equiv (1+(1-\alpha_{\rm PPD})\frac{q^2}{m_\pi^2})/\alpha_{\rm PPD}$. It is clear that the residual q^2-dependence becomes large as m_π^2 goes to zero. This feature is in agreement with what we observe in Fig.25. If we multiply the ratio by the corresponding factor $\Delta_{\rm PPD}(q^2)$, which is evaluated with measured $\alpha_{\rm PPD}$ and m_π, the linear-like q^2-dependence indeed disappears as indicated in Fig.26. Four different q^2 points of this ratio reveal q^2 independent plateau within their statistical errors. We then can evaluate the weighted average by using all four measured q^2 points to obtain the value of $G_P(q^2)/F_P^{\rm ren}(q^2)$ in the limit of $q^2 \to 0$, which corresponds to $m_\pi^2/(2m_{\rm AWT}\alpha_{\rm PPD})$.

Although $G_P(0)/F_P^{\rm ren}(0)$ is associated with the bare value of the low-energy constant B_0 in the pion-pole dominance model as discussed in Appendix B, this prediction is slightly modified as

$$\lim_{q^2\to 0}\frac{G_P(q^2)}{F_P^{\rm ren}(q^2)} = \frac{1}{\alpha_{\rm PPD}}\frac{m_f+m_{\rm res}}{m_f+m_{\rm shift}}B_0, \tag{66}$$

where the low-energy constant B_0 is defined by the relation $m_\pi^2 = 2(m_f+m_{\rm res})B_0$. Because of the fact that $m_{\rm res} \neq m_{\rm shift}$, the values of $G_P(0)/F_P^{\rm ren}(0) \times \alpha_{\rm PPD}$ deviate from B_0 as shown in Fig. 27. The horizontal solid and dashed lines represent the reference value of B_0 and its standard deviation, which are evaluated from fitting squared pion masses to the linear function $c_0 + c_1 \cdot m_f$. The fit yields the low-energy constant $B_0 = c_1/2 = 2.0705(93)$ in lattice units. The ratio of fitting parameters c_0 and c_1 gives rise to the value of $1.75(15) \times 10^{-3}$, which slightly overestimates $m_{\rm res}$ quoted in Ref. [20]. This is simply because our fitting is performed in the rather heavier quark mass region ($0.02 \le m_f \le 0.08$). For comparison, values of $m_\pi^2/2m_f$ and $m_\pi^2/2(m_f+m_{\rm res})$ are also plotted as square and circle symbols in Fig. 27. This observation may raise a question whether the single universal "residual mass" parameter exists. However, what we observe here is very sensitive to the correct chiral behavior of the nucleon matrix elements. The quenched approximation may provide unknown quenching effects in nucleon matrix elements near the chiral limit. In this sense, dynamical simulations are much preferable to investigate it further.

V. FINITE VOLUME EFFECT ON NUCLEON FORM FACTORS

As we discussed in Sec. III C, we have found a significant finite volume effect on the axial-vector coupling g_A, while there is no appreciable effect on the vector-coupling g_V. In this section, we test for finite volume effects on all of the five nucleon form factors computed in this study. Unlike those couplings g_V and g_A, which are defined at $q^2 = 0$, it is hard to compare values of the form factor at non-zero q^2 among different spatial sizes L. This is simply because non-zero q^2 values are discrete in units of $(2\pi/L)^2$. In this study, however, our largest spatial size ($L = 24$) is twice as large as the smallest one ($L = 12$). The q^2 value for $\mathbf{q} = \frac{2\pi}{L}(2,0,0)$ at $L = 24$ coincides with the one for $\mathbf{q} = \frac{2\pi}{L}(1,0,0)$ at $L = 12$. Therefore, at least, a single value of non-zero q^2 is common between two different lattice sizes.

In Fig. 28, we show results for the vector form factor $F_V(q^2)$ for three spatial sizes. The left (right) panel is for $m_f = 0.04$ ($m_f = 0.08$). Different symbols represent the values obtained from simulations with different spatial lattice sizes. Solid curves are dipole form fits results on the largest volume ($L = 24$) as we described in Sec.IV A 1. These curves should be capable of exposing finite volume effects on the form factor. Data points from smaller lattice sizes of either $L = 16$ or $L = 12$ at heavier m_f agree well with the dipole fits, while results obtained from the smallest lattice

($L = 12$) at lighter m_f seem to be slightly away from them. However, the values obtained from $L = 24$ and $L = 12$ at $q^2 \approx 0.44$ GeV are not significantly different in the statistical sense.

We next show the same type of figures for the induced tensor form factor $F_T(q^2)$ in Fig. 29. Qualitative features are quite similar to the case of the vector form factor. In the case of the heavier quark mass ($m_f = 0.08$), all data points follow the solid curve fairly well, which is the dipole form fitted to the data of the largest volume ($L = 24$). On the other hand, at lighter quark mass ($m_f = 0.04$), the data points obtained from the smallest lattice volume ($L = 12$) slightly overestimate the solid curve. Again, the value for $L = 12$ at $q^2 \approx 0.44$ GeV^2 is not significantly away from the value for $L = 24$ in the statistical sense.

Next, let us examine two form factors in the axial-vector channel, where the axial-vector coupling g_A significantly suffers from the finite volume effect. In Fig. 30, the axial-vector form factor $F_A(q^2)/F_A(0)$ for three spatial sizes is shown. Gross features are mostly similar to both the vector form factor and the induced tensor form factor. At the heavier quark mass, it is observed that all data points follow the solid curve fitted to data of the largest volume with the dipole form (44). Although two values at $q^2 \approx 0.44$ GeV^2 obtained from both largest and smallest volumes agree each other within statistical errors, the finite volume effect seems to be non-negligible in the lighter quark mass region. On the other hand, the finite volume effects do not show up in the induced pseudo-scalar form factor except for the lowest q^2 value for $L = 16$, as indicated in Fig. 31. The solid curves are obtained by fitting data of the largest volume with the PPD-like form (47), where the pion-pole structure is essential at low q^2. At this moment, we do not have any explanation why the lowest q^2 data for $L = 16$ deviates from the solid curve. We also show the form factor in the pseudo-scalar channel, namely $G_P(q^2)$, for three lattice sizes in Fig. 32. At either quark mass $m_f = 0.04$ or 0.08, all data points agree well with the solid curves fitted to data of the largest volume by the modified PPD form (63). All data that appear in Fig. 28-32 are tabulated in Tables XI-XIII.

Although we may observe the common tendency that the three form factors $F_V(q^2)$, $F_T(q^2)$ and $F_A(q^2)$ become flatter as a function of q^2 in the smallest volume ($L = 12$), we do not make a definite conclusion through this study. Rather we can say that the finite volume effects on the values of any form factor at finite q^2 are less appreciable than our expectation raised by the fact that the axial-vector coupling significantly suffers from the finite volume effect. Indeed, we could attempt the direct comparison between results for two lattice sizes only at $q^2 \approx 0.44$ GeV^2, which is a relatively high value. Therefore, we deduce that the finite volume effects are not so serious in the high q^2 region. Finally, it is worth mentioning that we confirm that our observed forms for the five form factors well describe the q^2-dependence of those form factors even in the relatively high q^2 region, up to at least $q^2 \approx 1.0$ GeV^2, apart from consideration of finite volume effects.

VI. COMPARISON WITH PREVIOUS RESULTS

As we discussed in Sec. IV, the larger spatial volume enables us to perform the shorter q^2-extrapolation to extract fundamental information on the nucleon structure, e.g. the magnetic moment, the charge radius and the induced pseudo-scalar coupling from respective form factors without large systematic uncertainties. However, some of previous studies are performed on relatively small volumes, where the longer q^2-extrapolation is inevitable. In this context, our lattice setup is superior to previous studies. (See Table XIV for a summary of previous calculations [2, 4, 5, 7].)

A large volume simulation, which is comparable to our lattice volume, $(3.6 \text{ fm})^3$, has been done by the LHPC Collaboration with the mixed action simulation using DWF valence quarks on the asqtad-improved gauge configurations with fourth-rooted staggered sea quarks. The quenching effect in our simulations could be observed through a comparison with the mixed action results. However, there is no detailed analysis of the usual form factors in Ref [5]. Instead, we can access their raw data of four nucleon form factors from their tables. We simply compare our measured form factors at the lightest quark mass (m_π=0.39 GeV) with their results with the lightest pion mass of 0.35 GeV and the largest volume of $(3.5 \text{ fm})^3$ in Fig. 33. Surprisingly, all figures for four form factors show good consistency between our quenched results and the LHPC mixed action results within statistical errors, at least, in the low q^2 region. This indicates that (un)quenching effects on these form factors are still small for $m_\pi \gtrsim 0.35$ GeV. However, this conclusion is rather premature since the mixed action simulation is *not* a fully dynamical simulation, rather a partially quenched simulation [51]. We must wait for fully dynamical DWF simulation to make a firm conclusion. The RBC and UKQCD Collaborations have begun 2+1 flavor DWF calculations with large physical volume [52, 53]. We will do such a comparison in a future publication.

Finally, it is worth comparing our DWF results with the results obtained using Wilson fermions. In Table XV, our results of the axial-vector coupling g_A and the rms radii of the iso-vector Dirac and Pauli form factors, the iso-vector nucleon magnetic moment $\mu_p - \mu_n$, the axial dipole mass, the induced pseudo-scalar coupling g_P and the pion-nucleon coupling $g_{\pi NN}$ in the chiral limit are compared with previous quenched Wilson results from Refs. [4] and [7]. Their lightest pion mass of 0.41 GeV and physical volume of $(2.9 \text{ fm})^3$ are relatively similar to our lattice set up. One finds that the rms radii and the axial dipole mass are quite consistent with each other, while the better agreement with the

experiment for the axial-vector coupling and the iso-vector nucleon magnetic moment appear in our quenched DWF results. Note that although the induced pseudo-scalar form factor $F_P(q^2)$ was calculated in Ref. [7], the value of the induced pseudo-scalar coupling g_P was not evaluated there.

Let us estimate g_P from their fit parameters given in Table III of Ref. [7] as follows. First we read off $\alpha_{\rm PPD}$ from their parameters obtained by the monopole fit $c_0/(1+q^2/\Lambda^2)$ to the ratio of $2M_N F_P(q^2)/F_A(q^2)$. The authors reported that the monopole mass Λ is larger than their measured pion mass, while the value of c_0 is smaller than $4M_N^2/m_\pi^2$ evaluated by the measured pion and nucleon masses. Therefore, their $\alpha_{\rm PPD}$ may have appreciable q^2-dependence, which is given by $(1+q^2/m_\pi^2)/(1+q^2/\Lambda^2)$. On the other hand, the value of $\alpha_{\rm PPD}$ at $q^2=0$ can be given by $c_0 m_\pi^2/(4M_N^2)$, which is ranged from 0.68 to 0.62 when the pion mass vary from 0.56 GeV to 0.41 GeV. There is the descending tendency with the decrease of the pion mass. A simple linear extrapolation with respect to the pion mass squared leads to a value in the chiral limit less than 0.6, that is significantly deviated from unity. Thus, one may easily deduce that their g_P should be much smaller than our observed g_P since their corresponding $\alpha_{\rm PPD}$ and measured $F_A(0)$, both of which are main ingredients in Eq. (48), are about 40% and 20% smaller than our DWF values respectively. Indeed, our quoted g_P of the quenched Wilson results in Table XV, which is determined with the value of $\alpha_{\rm PPD}$ evaluated at $q^2 = 0.88 m_\mu^2$, is almost a half of our quenched DWF value. This discrepancy is attributed to the fact that the Wilson fermions do not yield the correct pion-pole structure of $F_P(q^2)$ [7], while the PPD form provides a good description of the q^2-dependence of $F_P(q^2)$ at low q^2 in our DWF calculation.

VII. CONCLUSION

In this paper, we have studied the weak nucleon form factors at low q^2 in quenched lattice QCD. We have used domain wall fermions in a very large physical volume $(3.6\ \text{fm})^3$. There are two reasons for requiring such large volume. As shown in the early calculation of the axial-vector coupling g_A [15], the nucleon matrix element may suffer significantly large finite volume effects. However, we really did not know whether the spatial volume $(2.4\ \text{fm})^3$, that was utilized in Ref. [15], was large enough for the nucleon. Secondly, the large spatial extent provides the capability to access lower non-zero momentum transfer. For the spatial volume $(3.6\ \text{fm})^3$, the smallest value of non-zero q^2 is about $0.1\ \text{GeV}^2$.

We first demonstrated that the finite volume effect on the axial-vector coupling g_A is well described by the power-law behavior, while the vector coupling g_V has no appreciable finite volume effect. However, it is found that a serious finite volume effect on the axial-vector coupling g_A is not seen in the range of the spatial lattice size from 2.4 fm to 3.6 fm. Finally, we obtain the ratio of the axial-vector to the vector coupling $(g_A/g_V)^{\rm ren} = 1.219 \pm 0.038(\text{stat}) \pm 0.024(\text{norm}) \pm 0.002(\text{vol})$ at the physical point from the largest volume $(3.6\ \text{fm})^3$, which agrees with our early estimate from the volume $(2.4\ \text{fm})^3$ [15] and underestimates the experimental value of 1.2695(29) by less than 5%.

Using the largest volume $(3.6\ \text{fm})^3$, we studied four of the weak nucleon form factors and also the pseudo-scalar form factor. The q^2-dependences of all measured form factors at low q^2 are discussed with great interest [62]. It is observed that the vector (F_V), induced tensor (F_T) and the axial-vector (F_A) form factors are well described by the dipole form as $F_i(q^2) = F_i(0)/(1+q^2/M_i^2)$ $(i = V, T, A)$ at low q^2 ($q^2 < 0.44\ \text{GeV}^2$). Each measured dipole mass overestimates the corresponding experimental value by about 20 %. This fact indicates that corresponding rms radii are somewhat smaller than the actual nucleon size. However, interestingly, the ratios of dipole masses, $M_A/M_V = 1.285 \pm 0.073$ and $M_T/M_V = 0.869 \pm 0.057$ are fairly consistent with respective experimental ones. We also calculated the difference of the proton and neutron magnetic moments, $\mu_p - \mu_n = 4.13 \pm 0.23$, from the value of $F_T(q^2)$ at $q^2 = 0$. Our obtained value is about 14% smaller than experimental value of 4.70589.

We have presented a detailed study of the induced pseudo-scalar form factor $F_P(q^2)$, which is less well-known experimentally. It is observed that the q^2-dependence of $F_P(q^2)$ exhibits the strong quark-mass dependence in the low q^2 region. This is associated with the pion-pole contribution. Indeed, we confirm that the measured value of $F_P(q^2)$ is well described by the pion-pole dominance (PPD) form $F_P^{\rm PPD}(q^2) = 2M_N F_A(q^2)/(q^2+m_\pi^2)$ with a multiplicative factor $\alpha_{\rm PPD}(< 1)$. With the help of such the PPD-like form, we can evaluate the induced pseudo-scalar coupling as $(g_P)^{\rm ren} = 8.15 \pm 0.54(\text{stat}) \pm 0.16(\text{norm})$. This value is to be compared with the most recent experimental value of 7.3 ± 1.1 from the MuCap experiment. Furthermore, we evaluated the pion-nucleon coupling $g_{\pi NN}$ from the residue of the pion pole in the induced pseudo-scalar form factor and found $g_{\pi NN} = 10.4 \pm 1.0(\text{stat})$.

We have also studied the axial Ward-Takahashi identity in terms of the nucleon matrix elements, which may be referred to as the generalized Goldberger-Treiman relation. For this purpose, we also calculated the pseudo-scalar matrix element, which is described by the single form factor called as the pseudo-scalar form factor $G_P(q^2)$. We have found that the measured q^2-dependence of $G_P(q^2)$ is quite consistent with an expected behavior associated with $F_A(q^2)$ and $F_P(q^2)$ in consequence of the axial Ward-Takahashi identity, or the generalized Goldberger-Treiman relation. This fact ensures that the PPD form provides a good description of the q^2-dependence of $G_P(q^2)$ as well.

In the case of large but finite fifth dimension, the axial Ward-Takahashi identity for domain wall fermions can be

slightly modified by introducing an additive shift of the quark mass due to the presence of the midpoint contribution to the divergence of the axial-vector current. Such an additive constant shift known as the residual quark mass is usually measured through mesonic two-point correlation functions. In an earlier calculation, the residual quark mass is observed much smaller than the lightest quark mass utilized here [20]. However, our observed quark mass shift $m_{\rm shift}$, which is required for satisfaction of the generalized Goldberger-Treiman relation, is close to 50% of our lightest quark mass and an order of magnitude larger than the residual mass quoted in Ref. [20]. This issue may be connected with the correct chiral behavior of the nucleon matrix elements. In the quenched approximation, there may be unknown quenching effects in nucleon matrix elements in the vicinity of the chiral limit. In this context, the above issue is beyond the scope of this quenched study. Rather, dynamical simulations are much preferable to investigate it further. The RBC and UKQCD Collaborations have begun $N_f = 2 + 1$ flavor domain wall fermion calculations with large physical volume $V \approx (2.7\ {\rm fm})^3$ and the lightest ud quark mass down to 1/7 the strange quark mass ($m_\pi \approx 330$ MeV) [52]. We plan to develop the present calculation for a precise determination of nucleon form factors and also to address all of unsolved issues described in this paper. Such planning is now underway [53].

Note added: After the completion of this work, we became aware of a paper [7] where the nucleon axial-vector form factor $F_A(q^2)$ and induced pseudo-scalar form factor $F_P(q^2)$ are calculated in quenched and unquenched lattice QCD using Wilson fermions.

Acknowledgments

It is a pleasure to acknowledge S. Choi for his private communication providing actual values of the form factor $F_P(q^2)$ in his experiment. We would like to thank our colleagues in the RBC collaboration and especially T. Blum for helpful suggestions and his careful reading of the manuscript, and H.-W. Lin and S. Ohta for fruitful discussions. We also thank RIKEN, Brookhaven National Laboratory and the U.S. DOE for providing the facilities essential for the completion of this work. The results of calculations were performed by using of QCDOC at RIKEN BNL Research Center. S.S. is supported by the JSPS for a Grant-in-Aid for Scientific Research (C) (No. 19540265). T.Y. is supported by US DOE grant DE-FG02-92ER40716 and the University of Connecticut.

Appendix A: Various rms radii in the vector channel

In Table I, the electric charge and magnetization radii for the proton and neutron are summarized. Using these experimental values, the iso-vector electric charge and iso-vector magnetization radii can be evaluated by the following relations [4, 8]

$$\langle (r_E^v)^2 \rangle \equiv -6 \frac{1}{G_E^v(q^2)} \frac{dG_E^v(q^2)}{dq^2}\bigg|_{q^2=0} = \langle (r_E^p)^2 \rangle - \langle (r_E^n)^2 \rangle, \tag{67}$$

$$\langle (r_M^v)^2 \rangle \equiv -6 \frac{1}{G_M^v(q^2)} \frac{dG_M^v(q^2)}{dq^2}\bigg|_{q^2=0} = \frac{\mu_p}{\mu_v}\langle (r_M^p)^2 \rangle - \frac{\mu_n}{\mu_v}\langle (r_M^n)^2 \rangle, \tag{68}$$

where $G_{E(M)}^v(q^2) = G_{E(M)}^p(q^2) - G_{E(M)}^n(q^2)$ and $\mu_v = \mu_p - \mu_n$. Then one obtains $\sqrt{\langle (r_E^v)^2 \rangle} = 0.939(5)$ fm and $\sqrt{\langle (r_M^v)^2 \rangle} = 0.862(14)$ fm. Similarly, the rms radii for the iso-vector Dirac form factor $F_1^v(q^2) = F_1^p(q^2) - F_1^n(q^2)$ and the iso-vector Pauli form factor $F_2^v(q^2) = F_2^p(q^2) - F_2^n(q^2)$ can be given through the following relations [4, 8]:

$$\langle (r_1^v)^2 \rangle = \langle (r_E^v)^2 \rangle - \frac{3}{2}\frac{F_2^v(0)}{M_N^2}, \tag{69}$$

$$\langle (r_2^v)^2 \rangle = \frac{1}{\mu_v - 1}\left(\mu_v \langle (r_M^v)^2 \rangle - \langle (r_1^v)^2 \rangle\right), \tag{70}$$

which yield $\sqrt{\langle (r_1^v)^2 \rangle} = 0.797(4)$ fm and $\sqrt{\langle (r_2^v)^2 \rangle} = 0.879(18)$ fm.

Appendix B: Generalized Goldberger-Treiman relation and pion-pole dominance

The generalized Goldberger-Treiman relation is derived from the nucleon matrix elements of the currents on both sides of the axial Ward-Takahashi identity [24]; $\partial_\alpha A_\alpha^a(x) = 2\hat{m} P^a(x)$ where the exact iso-spin symmetry is considered

as $\hat{m} = m_u = m_d$. The nucleon matrix element of the divergence of the axial-vector current is represented in the following form:

$$\begin{aligned}\langle N(p')|\partial_\alpha A^a_\alpha(0)|N(p)\rangle &= \bar{u}_{_N}(p')[i(\not{p}-\not{p}')F_A(q^2) - q^2 F_P(q^2)]\gamma_5 t^a u_{_N}(p) \\ &= [2M_N F_A(q^2) - q^2 F_P(q^2)]\bar{u}_{_N}(p')\gamma_5 t^a u_{_N}(p). \end{aligned} \tag{71}$$

Here, it is worth mentioning that we have used the Dirac equation for the nucleon, $\bar{u}_{_N}(p)(i\not{p}+M_N) = (i\not{p}+M_N)u_{_N}(p) = 0$ to get from the first line to the second line. Then one easily finds that the q^2-dependences of three form factors are constrained by the following relation

$$2M_N F_A(q^2) = q^2 F_P(q^2) + 2\hat{m} G_P(q^2), \tag{72}$$

which is a consequence of the axial Ward-Takahashi identity. This expression may be referred to as the generalized Goldberger-Treiman relation [24].

Here we discuss the case where the limits $\hat{m} \to 0$ and $q^2 \to 0$ are taken on Eq.(72). Of course, the left-hand side (l.h.s.) of Eq.(72) yields a non-zero value in the double limit. First, we consider the case where the chiral limit is first taken before the limit of $q^2 \to 0$.

$$\lim_{q^2\to 0}\left(\lim_{\hat{m}\to 0} 2M_N F_A(q^2)\right) = \lim_{q^2\to 0}\left(q^2 \lim_{\hat{m}\to 0} F_P(q^2)\right), \tag{73}$$

which requires the massless pion pole in $F_P(q^2)$ in the chiral limit [35] as $\lim_{\hat{m}\to 0} F_P(q^2) \propto \frac{1}{q^2}$ for non-vanishing of the l.h.s. of Eq. (73). Secondly, the chiral limit is taken after the limit of $q^2 \to 0$:

$$\lim_{\hat{m}\to 0}\left(\lim_{q^2\to 0} 2M_N F_A(q^2)\right) = \lim_{\hat{m}\to 0}\left(2\hat{m} \lim_{q^2\to 0} G_P(q^2)\right), \tag{74}$$

which requires the $1/\hat{m}$ singularity in $G_P(q^2)$ at $q^2 = 0$ as $\lim_{q^2\to 0} G_P(q^2) \propto \frac{1}{\hat{m}} \sim \frac{1}{m_\pi^2}$ for non-vanishing of the l.h.s. of Eq. (74). As a result, $F_P(q^2)$ and $G_P(q^2)$ must have the pion-pole structure which should become dominant at low q^2 [35]. Therefore, one can deduce that $F_P(q^2)$ and $G_P(q^2)$ are described by the following forms, at least, in the vicinity of the pole position $q^2 = -m_\pi^2$ [35, 49].

$$F_P^{\rm PPD}(q^2) = \frac{2M_N F_A(q^2)}{q^2 + m_\pi^2}, \tag{75}$$

$$2\hat{m} G_P^{\rm PPD}(q^2) = 2M_N F_A(q^2)\frac{m_\pi^2}{q^2 + m_\pi^2}, \tag{76}$$

which we call the pion-pole dominance (PPD) forms. Consequently, we realize that the ratio of $G_P^{\rm PPD}(q^2)$ and $F_P^{\rm PPD}(q^2)$ gives the low-energy constant B_0 as

$$\frac{G_P^{\rm PPD}(q^2)}{F_P^{\rm PPD}(q^2)} = B_0, \tag{77}$$

where $m_\pi^2 = 2\hat{m}B_0$.

[1] For recent reviews, see K. Orginos, PoS **LAT2006**, 018 (2006), P. Hägler, PoS **LAT2007**, 013 (2007) and references therein.
[2] M. Göckeler *et al.*, [QCDSF Collaboration], Phys. Rev. D **71**, 034508 (2005).
[3] P. Hägler *et al.*, [LHPC collaboration], Phys. Rev. D **68**, 034505 (2003).
[4] C. Alexandrou, G. Koutsou, J. W. Negele and A. Tsapalis, Phys. Rev. D **74**, 034508 (2006).
[5] Ph. Hägler *et al.* [LHPC Collaborations], arXiv:0705.4295 [hep-lat].
[6] K. F. Liu, S. J. Dong, T. Draper and W. Wilcox, Phys. Rev. Lett. **74**, 2172 (1995).
[7] C. Alexandrou, G. Koutsou, T. Leontiou, J. W. Negele and A. Tsapalis, arXiv:0706.3011 [hep-lat].
[8] A. W. Thomas and W. Weise, "The Structure of the Nucleon," *Berlin, Germany: Wiley-VCH (2001) 389 p.*
[9] V. Bernard, L. Elouadrhiri and U. G. Meissner, J. Phys. G **28**, R1 (2002).
[10] T. Gorringe and H. W. Fearing, Rev. Mod. Phys. **76**, 31 (2004).
[11] V. A. Andreev *et al.* [MuCap Collaboration], arXiv:0704.2072 [nucl-ex].
[12] S. Choi *et al.*, Phys. Rev. Lett. **71**, 3927 (1993).
[13] M. L. Goldberger and S. B. Treiman, Phys. Rev. **110**, 1178 (1958).
[14] S. Sasaki, T. Blum, S. Ohta and K. Orginos, Nucl. Phys. Proc. Suppl. **106**, 302 (2002).
[15] S. Sasaki, K. Orginos, S. Ohta and T. Blum, Phys. Rev. D **68**, 054509 (2003).
[16] D. B. Kaplan, Phys. Lett. B **288**, 342 (1992).
[17] Y. Shamir, Nucl. Phys. B **406**, 90 (1993).
[18] V. Furman and Y. Shamir, Nucl. Phys. B **439**, 54 (1995).
[19] T. Blum *et al.*, Phys. Rev. D **69**, 074502 (2004).
[20] Y. Aoki *et al.*, Phys. Rev. D **69**, 074504 (2004).
[21] T. Blum *et al.*, Phys. Rev. D **66**, 014504 (2002).
[22] W. M. Yao *et al.* [Particle Data Group], J. Phys. G **33**, 1 (2006).
[23] R. G. Edwards *et al.* [LHPC Collaboration], Phys. Rev. Lett. **96**, 052001 (2006).
[24] W. I. Weisberger, Phys. Rev. **143**, 1302 (1966).
[25] S. Weinberg, Phys. Rev. **112**, 1375 (1958).
[26] C. E. Hyde-Wright and K. de Jager, Ann. Rev. Nucl. Part. Sci. **54**, 217 (2004) and references therein.
[27] G. Kubon *et al.*, Phys. Lett. B **524**, 26 (2002).
[28] G. Bardin *et al.*, Phys. Lett. B **104**, 320 (1981).
[29] G. Jonkmans *et al.*, Phys. Rev. Lett. **77**, 4512 (1996).
[30] D. H. Wright *et al.*, Phys. Rev. C **57**, 373 (1998).
[31] J. H. D. Clark *et al.*, Phys. Rev. Lett. **96**, 073401 (2006).
[32] D. D. Bakalov, M. P. Faifman, L. I. Ponomarev and S. I. Vinitsky, Nucl. Phys. A **384**, 302 (1982).
[33] A. Czarnecki, W. J. Marciano and A. Sirlin, arXiv:0704.3968 [hep-ph].
[34] S. Choi (private communication).
[35] Y. Nambu, Phys. Rev. Lett. **4**, 380 (1960).
[36] T. Takaishi, Phys. Rev. D **54**, 1050 (1996).
[37] P. de Forcrand *et al.* [QCD-TARO Collaboration], Nucl. Phys. B **577**, 263 (2000).
[38] D. Galletly *et al.* [QCDSF Collaboration], PoS **LAT2005**, 363 (2006) [arXiv:hep-lat/0510050].
[39] Y. Aoki *et al.*, Phys. Rev. D **73**, 094507 (2006) [arXiv:hep-lat/0508011].
[40] Y. Aoki, C. Dawson, J. Noaki and A. Soni, Phys. Rev. D **75**, 014507 (2007) [arXiv:hep-lat/0607002].
[41] S. Gusken, Nucl. Phys. Proc. Suppl. **17** (1990) 361.
[42] C. Alexandrou, S. Gusken, F. Jegerlehner, K. Schilling and R. Sommer, Nucl. Phys. B **414**, 815 (1994).
[43] F. Berruto, T. Blum, K. Orginos and A. Soni, Phys. Rev. D **73**, 054509 (2006).
[44] S. Sasaki, T. Blum and S. Ohta, Phys. Rev. D **65**, 074503 (2002).
[45] K. Sasaki and S. Sasaki, Phys. Rev. D **72**, 034502 (2005).
[46] M. A. B. Beg and A. Zepeda, Phys. Rev. D **6**, 2912 (1972).
[47] T. E. O. Ericson, B. Loiseau and A. W. Thomas, Phys. Rev. C **66**, 014005 (2002).
[48] S. Sasaki and T. Yamazaki, in progress.
[49] S. L. Adler, Phys. Rev. **139**, 1638 (1965).
[50] S. Sasaki and T. Yamazaki, PoS **LAT2006**, 092 (2006).
[51] T. Yamazaki *et al.* [RBC+UKQCD Collaboration], Phys. Rev. Lett. **100**, 171602 (2008).
[52] P. Boyle [RBC Collaboration], PoS **LAT**, 005 (2007).
[53] T. Yamazaki and S. Ohta [RBC Collaboration], PoS **LAT2007**, 165 (2007).
[54] In this paper, we restrict ourselves to considering the iso-spin symmetric case as $m_u = m_d$, where the second-class form factors do not appear in consequence of G-parity invariance [25].
[55] The sign of all form factors is chosen to be positive. Remark that our γ_5 definition, $\gamma_5 \equiv \gamma_x\gamma_y\gamma_z\gamma_t = -\gamma_5^M$, has the opposite sign relative to that in the Minkowski convention ($\vec{\gamma}^M = i\vec{\gamma}$ and $\gamma_0^M = \gamma_t$) adopted in the particle data group [22].
[56] One might worry about the large scaling violation, which is observed for the axial-vector coupling g_A in a quenched calculation with overlap fermions at the same lattice spacing [38]. However, the previous quenched DWF studies reported that there is no appreciate scaling violation in the kaon B-parameter B_K [39] and proton decay matrix elements [40] at

$\beta = 0.87$ ($a \approx 0.15$ fm) and 1.04 ($a \approx 0.10$ fm). We may deduce that no large scaling violation is ensured for other matrix elements as well in our DWF calculations.
[57] We treat our data sets as 70 independent measurements after taking average of the multiple source results on each configuration.
[58] It is worth mentioning that such consistency is not observed at $L = 16$, since the lowest q^2 point at $L = 16$ may suffer from the finite volume effect as we will describe in Sec. V.
[59] Here we use a traditional convention as $F_\pi = f_\pi/\sqrt{2} \sim 93$MeV, while f_π is quoted in Ref.[20].
[60] Strictly speaking, the relativistic dispersion relation (18), which ensures that $(i\not{p} + M_N)u_N(p) = 0$, should be well satisfied in simulations.
[61] In Ref. [7], the similar deviation from unity as $\alpha_{\rm AWT} > 1$ can be read off from their Fig. 19 where an inverse of $\alpha_{\rm AWT}$ is given in the limit of $q^2 \to 0$.
[62] Detailed knowledge about the q^2-dependence of the weak form factors in neutron beta decay is required for our lattice study of flavor $SU(3)$ breaking effects in hyperon beta decays [50].

TABLE I: Experimental values of magnetic moments, electric charge and magnetization radii of the proton and neutron.

Observable	Experimental value	Reference
μ_p	$+2.792847351(28)$	[22]
μ_n	$-1.91304273(45)$	[22]
$\langle(r_E^p)^2\rangle^{1/2}$	0.8750(68) fm	[22]
$\langle(r_E^n)^2\rangle$	$-0.1161(22)$ fm^2	[22]
$\langle(r_M^p)^2\rangle^{1/2}$	0.855(35) fm	[26]
$\langle(r_M^n)^2\rangle^{1/2}$	0.873(11) fm	[27]

TABLE II: Summary of available experimental data for the induce pseudo-scalar form factor $F_P(q^2)$. The smallest q^2 point is given by the MuCap experiment, while other three q^2 points are obtained from a single experiment of pion electroproduction at threshold.

q^2 (GeV^2)	$F_P(q^2)$ (MeV^{-1})	Experiment (reference)
0.0098	0.069 ± 0.010	ordinary muon capture [11]
0.073	0.0229 ± 0.0028	pion electroproduction [12, 34]
0.139	0.0140 ± 0.0022	pion electroproduction [12, 34]
0.179	0.00932 ± 0.00248	pion electroproduction [12, 34]

TABLE III: Simulation parameters for each volume studied in this work.

Gauge action (β)	$L^3 \times T$	L_s	M_5	Quark mass values (m_f)	spatial size L [fm]	Statistics	# of sources
DBW2 (0.87)	$24^3 \times 32$	16	1.8	0.02, 0.04, 0.06, 0.08	3.6	70	3
	$16^3 \times 32$	16	1.8	0.04, 0.06, 0.08	2.4	377	1
	$12^3 \times 32$	16	1.8	0.04, 0.06, 0.08	1.8	800	1

TABLE IV: The residual mass $m_{\rm res}$, inverse lattice spacing (a_ρ^{-1}, set by the ρ meson mass), the renormalization factor of the axial-vector current (Z_A), and the pion decay constant (F_π). Those values are taken from Ref. [20], where simulations are performed on a $16^3 \times 32$ volume.

Gauge action (β)	M_5	L_s	$m_{\rm res}$	a_ρ^{-1} [GeV]	$Z_A(m_f = -m_{\rm res})$	F_π [MeV]
DBW2 (0.87)	1.8	16	$5.69(26)\times10^{-4}$	1.31(4)	0.77759(45)	91.2(5.2)

TABLE V: Fitted masses of the pseudo-scalar meson state and fitted energies of the nucleon state with the five lowest momenta for each volume. All tabulated values are given in lattice units. Results for the nucleon energies with nonzero momenta are averaged over all possible permutations of the lattice momentum $\mathbf{p} = (n_x, n_x, n_z)$ in units of $2\pi/L$, including both positive and negative directions.

			$E_N(\mathbf{p})$				
size L	m_f	m_π	(0, 0, 0)	(1,0,0)	(1,1,0)	(1,1,1)	(2,0,0)
24	0.02	0.3003 (10)	0.8651 (70)	0.9038 (79)	0.9432 (94)	0.9824 (117)	1.0157 (130)
	0.04	0.4143 (11)	0.9801 (52)	1.0152 (58)	1.0496 (66)	1.0829 (77)	1.1161 (83)
	0.06	0.5040 (11)	1.0783 (47)	1.1098 (50)	1.1408 (55)	1.1710 (60)	1.2006 (66)
	0.08	0.5829 (11)	1.1690 (43)	1.1976 (45)	1.2257 (49)	1.2531 (53)	1.2793 (57)
16	0.04	0.4148 (9)	0.9869 (50)	1.0595 (58)	1.1251 (74)	1.1822 (106)	1.2436 (150)
	0.06	0.5050 (8)	1.0821 (42)	1.1483 (48)	1.2095 (61)	1.2632 (84)	1.3189 (111)
	0.08	0.5837 (8)	1.1703 (37)	1.2313 (43)	1.2886 (54)	1.3391 (71)	1.3890 (92)
12	0.04	0.4150 (10)	0.9795 (75)	1.097 (10)	1.190 (17)	1.332 (68)	1.236 (79)
	0.06	0.5046 (9)	1.0729 (55)	1.1844 (70)	1.280 (12)	1.419 (41)	1.466 (22)
	0.08	0.5832 (8)	1.1703 (37)	1.2313 (43)	1.289 (54)	1.339 (71)	1.389 (92)

TABLE VI: Results for the vector coupling $g_V^{\rm lattice}$, the axial-vector coupling $g_A^{\rm lattice}$ and their ratio $g_A^{\rm ren} = (g_V/g_A)^{\rm lattice}$. Gauss-smeared-to-gauss-smeared quark propagators are used in the present study, while box-to-local quark propagators were used in the previous calculation [15]. $L = 16$ results in the present calculations agree well with the previous $L = 16$ results.

Smearing type (Ref.)	$L^3 \times N_t$	m_f	$(g_V)_{\rm lattice}$	$(g_A)_{\rm lattice}$	$(g_A)_{\rm ren}$
Gauss-Gauss (this work)	$24^3 \times 32$	0.02	1.2435(60)	1.509(52)	1.212(42)
		0.04	1.2386(18)	1.537(27)	1.240(22)
		0.06	1.2306(12)	1.533(18)	1.245(15)
		0.08	1.2206(10)	1.529(14)	1.252(11)
	$16^3 \times 32$	0.04	1.2429(24)	1.494(29)	1.202(24)
		0.06	1.2332(12)	1.497(17)	1.214(14)
		0.08	1.2224(9)	1.499(13)	1.226(11)
	$12^3 \times 32$	0.04	1.2465(34)	1.441(51)	1.156(41)
		0.06	1.2328(16)	1.462(27)	1.185(22)
		0.08	1.2213(11)	1.474(17)	1.206(14)
Box-Local [15]	$16^3 \times 32$	0.02	1.2440(30)	1.531(60)	1.229(49)
		0.04	1.2323(14)	1.523(24)	1.230(20)
		0.06	1.2220(10)	1.510(15)	1.230(12)
		0.08	1.2106(8)	1.505(11)	1.236(9)
	$8^3 \times 24$	0.04	1.223(10)	1.303(146)	1.059(120)
		0.06	1.214(5)	1.342(74)	1.099(62)
		0.08	1.203(4)	1.373(46)	1.136(39)

TABLE VII: Fitted results of $F_1(q^2)$ and $F_2(q^2)$ with the dipole form [Eqs.(37) and (39)] and their extrapolated values to the chiral limit and the physical point.

	$F_1(q^2) = F_V(q^2)$		$F_2(q^2) = 2M_N F_T(q^2)$		
m_f	M_V (GeV)	$\langle r_V^2\rangle^{\frac{1}{2}}$ (fm)	$F_2^{\rm ren}(0) = F_2(0)/F_V(0)$	M_T (GeV)	$\langle r_T^2\rangle^{\frac{1}{2}}$ (fm)
0.08	1.330(17)	0.514(7)	3.76(7)	1.155(18)	0.592(9)
0.06	1.286(21)	0.532(9)	3.65(9)	1.112(22)	0.615(12)
0.04	1.239(32)	0.552(14)	3.48(13)	1.072(32)	0.637(19)
0.02	1.177(65)	0.581(32)	3.08(26)	1.062(78)	0.644(47)
phys. point	1.148(55)	0.589(25)	3.13(23)	1.002(58)	0.676(34)
chiral limit	1.142(57)	0.592(25)	3.11(24)	0.997(60)	0.679(35)
Empirical values	0.857(8)	0.797(4)	3.70589	0.778(23)	0.879(18)

TABLE VIII: Fitted results of $F_A(q^2)$ with the dipole form [Eq.(37)] and $F_P(q^2)$ with the PPD-like form [Eq.(47)], and their extrapolated values to the chiral limit and the physical point.

	$F_A(q^2)$			$F_P(q^2)$	
m_f	$(g_A)^{\rm ren} = F_A(0)/F_V(0)$	M_A (GeV)	$\langle r_A^2\rangle^{\frac{1}{2}}$ (fm)	$(g_P)^{\rm ren}$	$\alpha_{\rm PPD}$
0.08	1.252(11)	1.572(26)	0.435(7)	11.08(28)	0.815(18)
0.06	1.245(15)	1.541(32)	0.444(9)	10.37(28)	0.831(18)
0.04	1.240(22)	1.523(47)	0.449(14)	9.66(34)	0.853(20)
0.02	1.212(42)	1.618(126)	0.422(33)	8.73(51)	0.884(31)
phys. point	1.219(38)	1.502(83)	0.453(24)	8.15(54)	0.897(32)
chiral limit	1.218(40)	1.500(85)	0.454(25)	8.04(55)	0.900(33)
Experimental values	1.2695(29)	1.026(21)	0.666(14)	7.3 (1.1)	1 (Theor.)

TABLE IX: Ratio of the dipole masses and their extrapolated values to the chiral limit and the physical point.

m_f	M_T/M_V	M_A/M_V
0.08	0.869(14)	1.182(17)
0.06	0.865(19)	1.198(24)
0.04	0.865(32)	1.229(42)
0.02	0.902(84)	1.374(131)
phys. point	0.869(57)	1.285(73)
chiral limit	0.869(58)	1.289(75)
Empirical values	0.908(28)	1.197(27)

TABLE X: Results of the ratio $\alpha_{\rm AWT}$, the quark mass ($m_{\rm AWT}$) defined in the generalized Goldberger-Treiman relation [Eq.(62)] and the mass shift $m_{\rm shift}$.

m_f	$\alpha_{\rm AWT}$	$m_{\rm AWT}$	$m_{\rm shift} = m_{\rm AWT} - m_f$
0.08	1.12(1)	0.0896(7)	0.0096(7)
0.06	1.15(1)	0.0688(7)	0.0088(7)
0.04	1.21(2)	0.0484(8)	0.0084(8)
0.02	1.41(6)	0.0281(12)	0.0081(12)
0	N/A	0.0073(12)	0.0073(12)

TABLE XI: Results of five (dimensionless) form factors computed on a $24^3 \times 32$ volume. All form factors are renormalized except for the pseudo-scalar form factor $G_P(q^2)$. For notational simplicity, we use the momentum $\mathbf{q}$ in units of $2\pi/L$.

m_f	$\mathbf{q}$	q^2 (GeV^2)	$F_V^{\rm ren}(q^2)$	$2M_N F_T^{\rm ren}(q^2)$	$F_A^{\rm ren}(q^2)$	$2M_N F_P^{\rm ren}(q^2)$	$G_P^{\rm bare}(q^2)$
0.02	(0,0,0)	0.000	1.0000(48)	N/A	1.212(42)	N/A	N/A
	(1,0,0)	0.113	0.852(15)	2.53(21)	1.132(41)	19.79(1.55)	21.75(1.11)
	(1,1,0)	0.222	0.739(23)	2.16(17)	1.040(40)	12.00(99)	15.26(79)
	(1,1,1)	0.326	0.633(29)	1.82(17)	0.892(40)	8.36(74)	11.76(78)
	(2,0,0)	0.427	0.617(42)	1.61(19)	0.921(62)	7.40(79)	8.88(1.01)
0.04	(0,0,0)	0.000	1.0000(15)	N/A	1.240(22)	N/A	N/A
	(1,0,0)	0.114	0.864(6)	2.88(11)	1.131(21)	15.61(81)	17.43(43)
	(1,1,0)	0.224	0.757(10)	2.42(10)	1.031(21)	10.97(50)	13.12(34)
	(1,1,1)	0.331	0.668(13)	2.06(9)	0.927(19)	8.20(43)	10.45(33)
	(2,0,0)	0.434	0.622(18)	1.83(10)	0.897(28)	6.91(47)	8.44(35)
0.06	(0,0,0)	0.000	1.0000(10)	N/A	1.245(15)	N/A	N/A
	(1,0,0)	0.114	0.872(4)	3.05(8)	1.133(14)	13.46(59)	14.66(25)
	(1,1,0)	0.225	0.771(6)	2.60(7)	1.036(14)	10.27(39)	11.60(20)
	(1,1,1)	0.333	0.687(8)	2.24(7)	0.946(13)	8.01(33)	9.53(20)
	(2,0,0)	0.439	0.633(11)	1.98(7)	0.895(18)	6.72(39)	7.87(22)
0.08	(0,0,0)	0.000	1.0000(8)	N/A	1.252(11)	N/A	N/A
	(1,0,0)	0.114	0.879(3)	3.18(6)	1.143(10)	12.29(53)	12.88(17)
	(1,1,0)	0.226	0.782(4)	2.74(6)	1.048(10	9.80(34)	10.51(14)
	(1,1,1)	0.335	0.702(6)	2.39(5)	0.963(10)	7.88(29)	8.82(14)
	(2,0,0)	0.442	0.645(8)	2.11(6)	0.905(14)	6.67(37)	7.41(17)

TABLE XII: The same as Table XI, but for a $16^3 \times 32$ volume.

m_f	$\mathbf{q}$	q^2 (GeV^2)	$F_V^{\rm ren}(q^2)$	$2M_N F_T^{\rm ren}(q^2)$	$F_A^{\rm ren}(q^2)$	$2M_N F_P^{\rm ren}(q^2)$	$G_P^{\rm bare}(q^2)$
0.04	(0,0,0)	0.000	1.0000(19)	N/A	1.202(24)	N/A	N/A
	(1,0,0)	0.251	0.718(15)	2.14(10)	0.939(23)	7.87(64)	12.54(45)
	(1,1,0)	0.485	0.565(19)	1.53(8)	0.751(30)	6.00(40)	7.45(36)
	(1,1,1)	0.706	0.430(25)	1.14(8)	0.645(35)	3.78(34)	5.04(35)
	(2,0,0)	0.915	0.417(49)	0.97(14)	0.558(64)	2.29(43)	4.53(59)
0.06	(0,0,0)	0.000	1.0000(10)	N/A	1.214(14)	N/A	N/A
	(1,0,0)	0.253	0.744(9)	2.37(7)	0.963(15)	8.00(52)	10.93(25)
	(1,1,0)	0.491	0.593(13)	1.80(5)	0.788(20)	6.04(27)	7.09(21)
	(1,1,1)	0.717	0.471(17)	1.33(6)	0.688(23)	4.17(25)	4.93(22)
	(2,0,0)	0.933	0.430(29)	1.06(9)	0.580(37)	2.48(32)	4.15(34)
0.08	(0,0,0)	0.000	1.0000(7)	N/A	1.226(11)	N/A	N/A
	(1,0,0)	0.254	0.760(7)	2.53(5)	0.988(11)	7.99(50)	9.92(18)
	(1,1,0)	0.495	0.611(10)	1.93(4)	0.816(15)	6.15(22)	6.76(15)
	(1,1,1)	0.725	0.496(13)	1.47(5)	0.714(17)	4.42(22)	4.83(16)
	(2,0,0)	0.946	0.440(20)	1.14(7)	0.599(27)	2.64(30)	3.98(25)

TABLE XIII: The same as Table XI, but for a $12^3 \times 32$ volume.

m_f	$\mathbf{q}$	q^2 (GeV^2)	$F_V^{\rm ren}(q^2)$	$2M_N F_T^{\rm ren}(q^2)$	$F_A^{\rm ren}(q^2)$	$2M_N F_P^{\rm ren}(q^2)$	$G_P^{\rm bare}(q^2)$
0.04	(0,0,0)	0.000	1.0000(27)	N/A	1.156(41)	N/A	N/A
	(1,0,0)	0.434	0.681(34)	2.02(14)	0.883(43)	7.47(74)	7.81(61)
	(1,1,0)	0.822	0.466(53)	1.32(16)	0.693(81)	3.44(56)	4.79(66)
0.06	(0,0,0)	0.000	1.0000(13)	N/A	1.185(22)	N/A	N/A
	(1,0,0)	0.439	0.672(17)	2.03(8)	0.885(23)	7.00(54)	7.60(33)
	(1,1,0)	0.837	0.468(25)	1.33(8)	0.666(38)	3.59(34)	4.41(30)
0.08	(0,0,0)	0.000	1.0000(9)	N/A	1.206(14)	N/A	N/A
	(1,0,0)	0.442	0.671(11)	2.09(6)	0.891(16)	6.74(48)	7.23(23)
	(1,1,0)	0.848	0.477(15)	1.38(5)	0.669(25)	3.74(25)	4.20(19)

TABLE XIV: Previous lattice calculations for nucleon form factors. Note that our lowest non-zero q^2 ($q^2_{\rm min}$) is smaller than previous calculations. This is an essential point in determinations of the induced pseudo-scalar coupling (g_P) from $F_P(q^2)$ and the nucleon magnetic moments (μ_N) from $F_T(q^2)$ in order to reduce the systematic uncertainties stemming from long q^2-extrapolation.

Group (reference)	Type	Fermion (valence)	a [fm]	spatial size [fm]	m_π [GeV]	$q^2_{\rm min}$ [GeV^2]
QCDSF [2] [a]	Quench	Clover	0.11	1.8	0.54, 0.64, 0.74, 0.91, 0.98	0.47
			0.08	1.9	0.61, 0.76, 0.89, 1.03	0.40
			0.06	1.9	0.63, 0.79, 0.79, 0.93, 1.05	0.39
Cyprus-MIT [4, 7]	Quench	Wilson	0.09	2.9	0.41, 0.49, 0.56	0.17
	Full ($N_f = 2$)	Wilson	0.08	1.9	0.38, 0.51,0.69	0.42
LHPC [5] [b]	Mixed ($N_f = 2+1$) [c]	DWF	0.124	3.5	0.35	0.11
			0.124	2.5	0.36, 0.50, 0.60, 0.68, 0.76	0.18−0.20
This work	Quench	DWF	0.15	3.6	0.39, 0.54, 0.66, 0.76	0.11
			0.15	2.4	0.54, 0.66, 0.76	0.25
			0.15	1.8	0.54, 0.66, 0.76	0.43

[a] Only electric-magnetic form factors (F_V, F_T) are studied.
[b] Raw data of F_V, F_T, F_A and F_P are available in tables, while detail analysis is not found.
[c] DWF valence quarks on the asqtad-improved gauge configurations with fourth-rooted staggered sea quarks.

TABLE XV: Comparisons with previous quenched Wilson results obtained from Refs. [4] and [7]. The extrapolated values in the chiral limit are evaluated by a simple linear quark mass dependence.

Reference	$\mu_p - \mu_n$	$\langle r_V^2 \rangle^{\frac{1}{2}}$ [fm]	$\langle r_T^2 \rangle^{\frac{1}{2}}$ [fm]	$(g_A)^{\rm ren}$	M_A [GeV]	$(g_P)^{\rm ren}$	$g_{\pi NN}$ [a]
Refs. [4] and [7]	3.73(13)	0.585(13)	0.72(2)	1.065(24) [b]	1.500(59) [b]	3.54(61) [c]	11.8(0.3)
This work	4.11(24)	0.592(25)	0.679(35)	1.218(40)	1.500(85)	8.04(55)	10.4(1.0)

[a] $g_{\pi NN}$ was evaluated at $q^2 = 0$ in Ref.[7], while our $g_{\pi NN}$ is defined at the pion pole, $q^2 = -m_\pi^2$ with the physical pion mass.
[b] The chiral extrapolated values are not available in Ref [7]. Therefore, we performed correlated fits with their measured data to evaluate them.
[c] Although $F_P(q^2)$ was calculated in Ref. [7], the value of the induced pseudo-scalar coupling was not evaluated. The quoted value is estimated by us as described in the text.

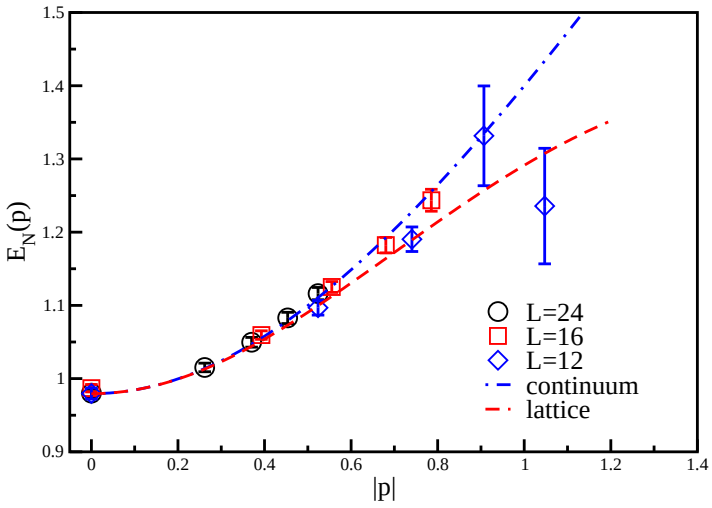

FIG. 1: Comparison of measured and estimated energies of the nucleon for $m_f = 0.04$ as a function of absolute value of three-momentum $|\mathbf{p}|$. Open circles, squares and diamonds, which corresponds to the measured values in lattice units, are obtained from $L = 24$, $L = 16$ and $L = 12$. The estimated energies are given by the relativistic dispersion formula $E(\mathbf{p}) = \sqrt{\mathbf{p}^2 + M_N^2}$ for continuum-like momenta $p_i = \frac{2\pi}{L} n_i$ (dashed-dotted curve) and lattice momenta $p_i = \sin[\frac{2\pi}{L} n_i]$ (dashed curve) with the rest mass M_N measured at $L = 24$.

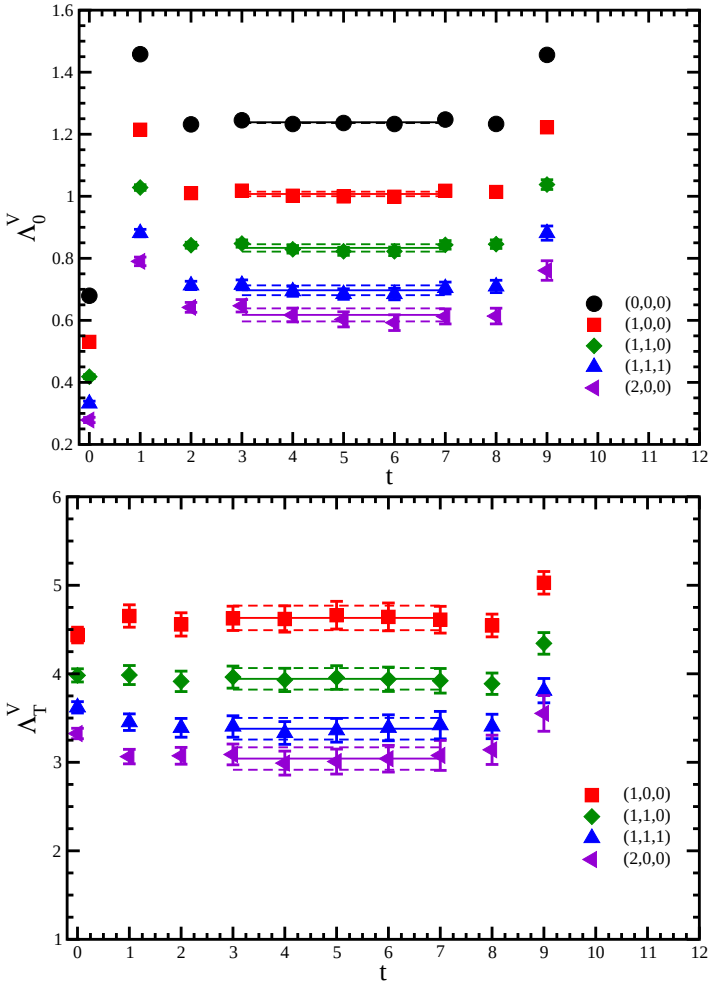

FIG. 2: Relevant ratios of three- and two-point functions, Λ_0^V (top) and Λ_T^V (bottom), for all possible three-momentum transfer $\mathbf{q}$ as a function of the current insertion time slice at $m_f = 0.04$.

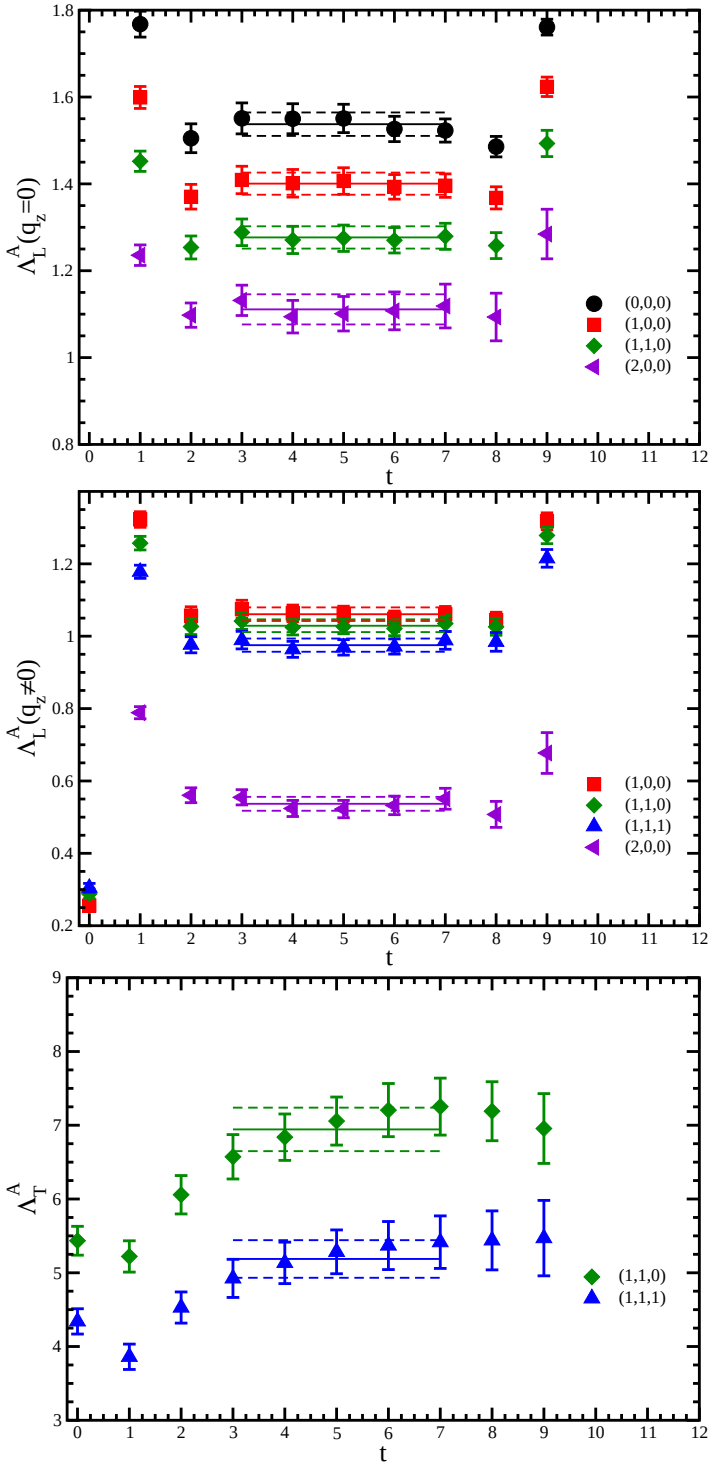

FIG. 3: Relevant ratios of three- and two-point functions, $\Lambda_L^A(q_z = 0)$ (top), $\Lambda_L^A(q_z \neq 0)$ (middle) and Λ_T^A (bottom), for all possible three-momentum transfer $\mathbf{q}$ as a function of the current insertion time slice at $m_f = 0.04$.

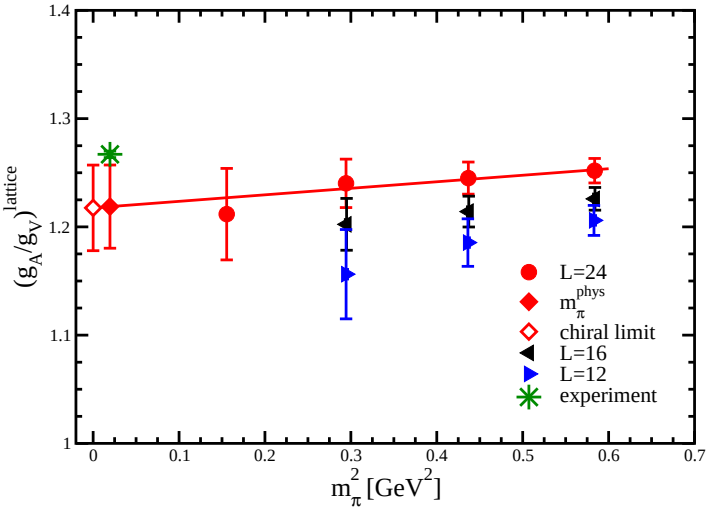

FIG. 4: The physical ratio of couplings g_A/g_V as a function of the pion mass squared. Results on the largest volume (3.6 fm)^3 (circles) exhibit milder quark mass dependence, while the smaller volume results (right-oriented triangles) show a slow downward tendency toward the chiral limit away from the experimental point (asterisk).

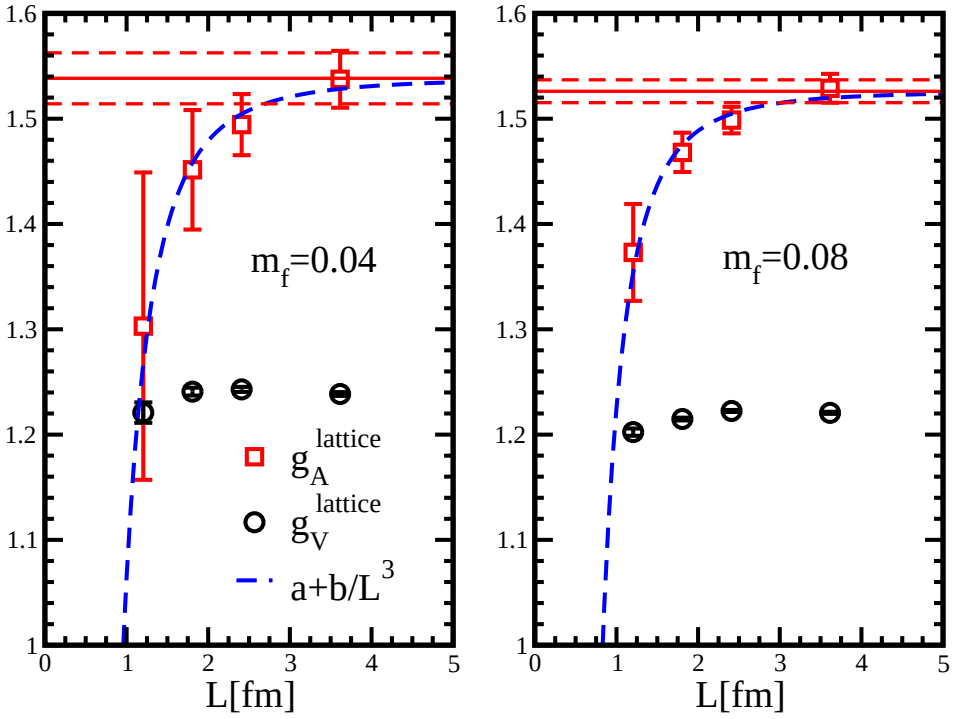

FIG. 5: The vector coupling $(g_V)^{\rm lattice}$ and axial-vector coupling $(g_A)^{\rm lattice}$ as functions of spatial lattice size for $m_f = 0.04$ (left figure) and $m_f = 0.08$ (right figure). Dashed curves are fits of the form $g_A^{\rm lattice}(L) = g_A^{\rm lattice}(\infty) + bL^{-3}$.

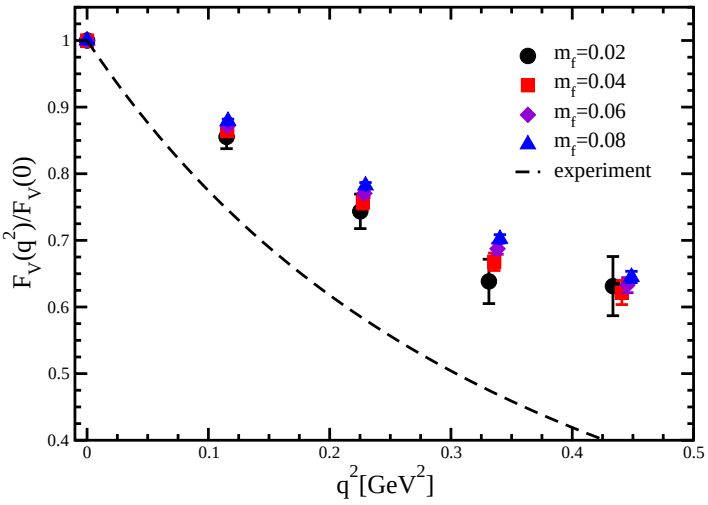

FIG. 6: The renormalized Dirac form factor, $F_V^{\rm ren}(q^2) = F_V(q^2)/F_V(0)$ as a function of four-momentum squared q^2.

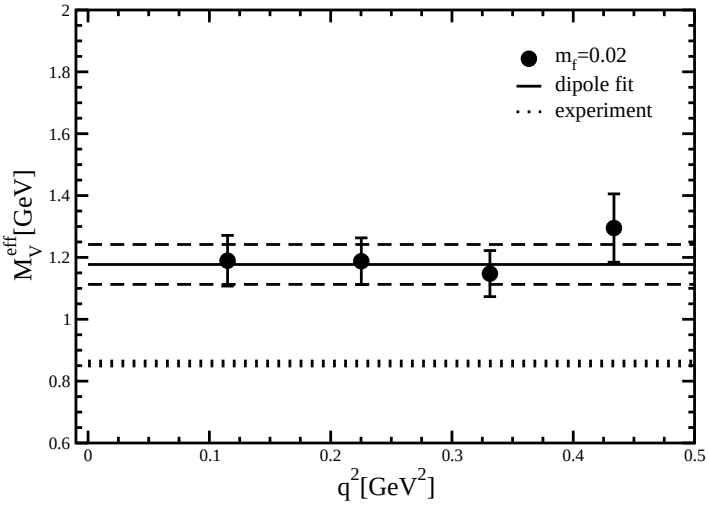

FIG. 7: Effective dipole-mass plot for the Dirac form factor $F_V(q^2)$ as a function of four-momentum squared q^2 at $m_f = 0.02$.

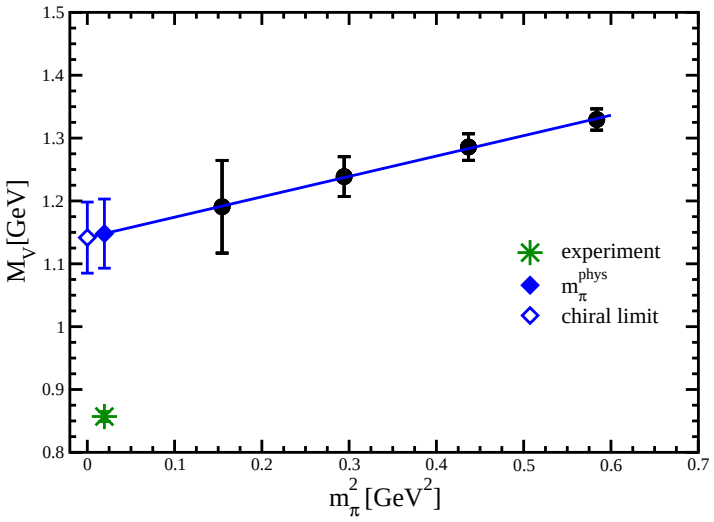

FIG. 8: Chiral extrapolation of the Dirac dipole mass M_V. The extrapolated points in the chiral limit and at the physical point are represented by an open diamond and a filled diamond. The experimental value is marked with an asterisk.

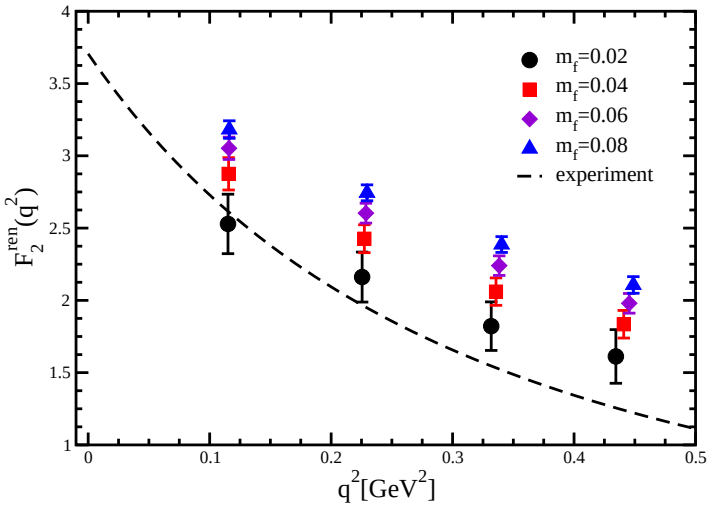

FIG. 9: The renormalized Pauli form factor, $F_2^{\rm ren}(q^2) = 2MF_T(q^2)/F_V(0)$ as a function of four-momentum squared q^2.

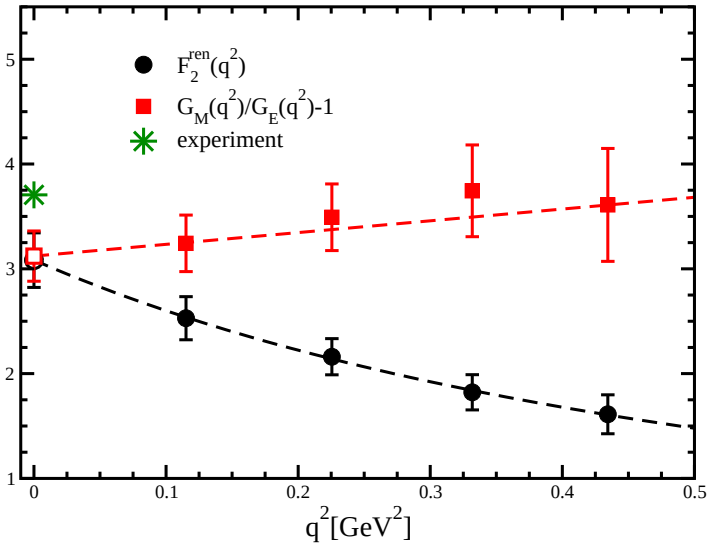

FIG. 10: The q^2 extrapolation toward $q^2 = 0$ for either $F_2^{\rm ren}(q^2)$ or $G_M(q^2)/G_E(q^2) - 1$ for $m_f = 0.02$. Those quantities should intersect each other at $q^2 = 0$. For $F_2^{\rm ren}(q^2)$, the dipole form is applied, while a simple linear extrapolation with respect to q^2 is used for $G_M(q^2)/G_E(q^2) - 1$ thanks to its mild q^2-dependence. The extrapolated values from both determinations agree well with each other, although those underestimate the experimental value.

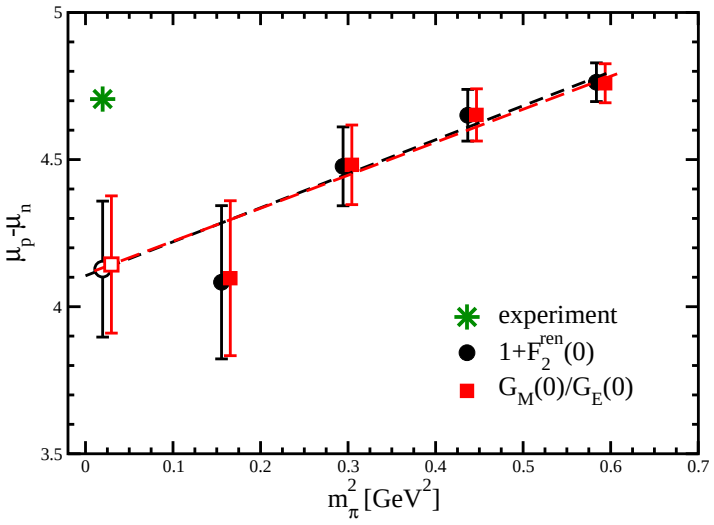

FIG. 11: Chiral extrapolation of $\mu_p - \mu_n$. The square symbols have been moved slightly in the plus x-direction.

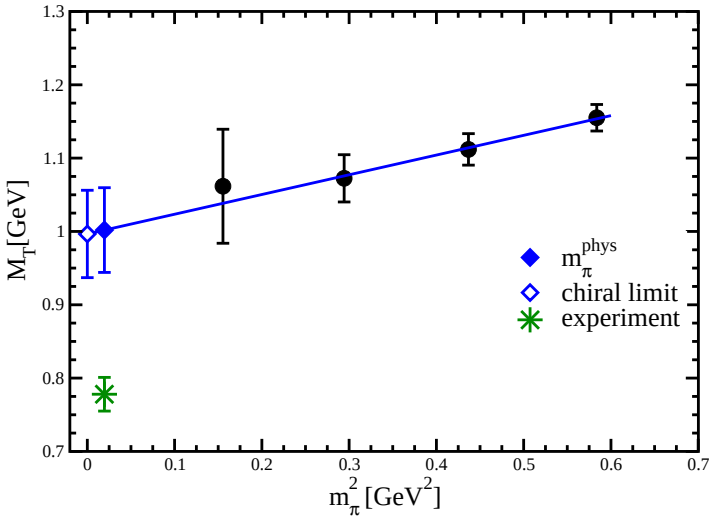

FIG. 12: Chiral extrapolation of the Pauli dipole mass M_T. Symbols are defined as in Fig. 8.

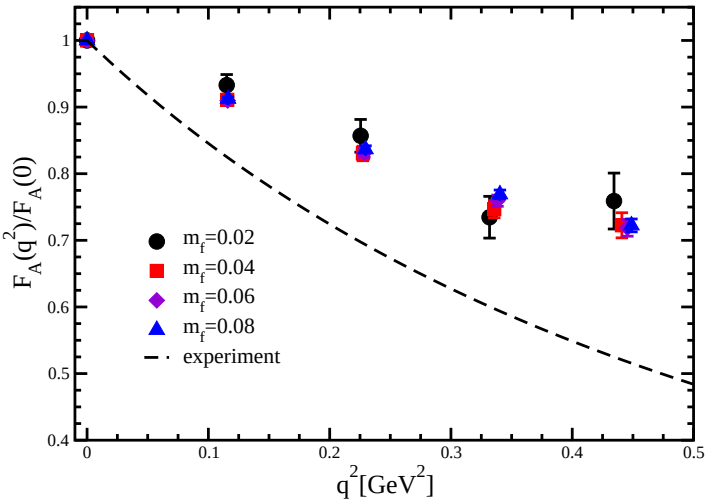

FIG. 13: The axial-vector form factor normalized by $F_A(0)$ as a function of four-momentum squared q^2.

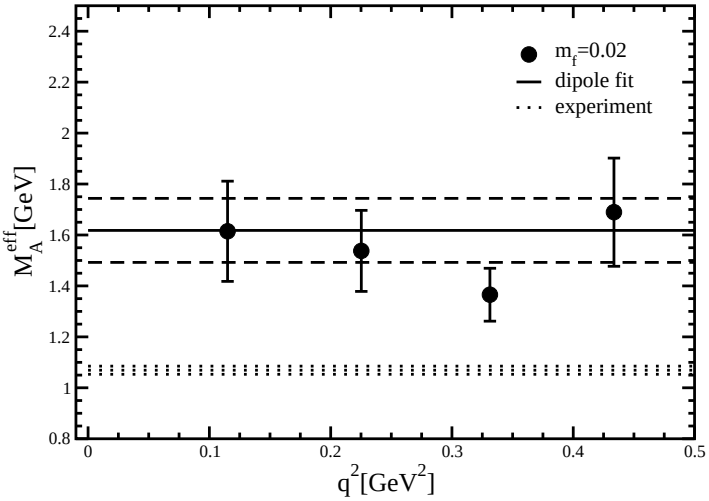

FIG. 14: Effective dipole-mass plot for the axial-vector form factor $F_A(q^2)$ as a function of four-momentum squared q^2 at $m_f = 0.02$.

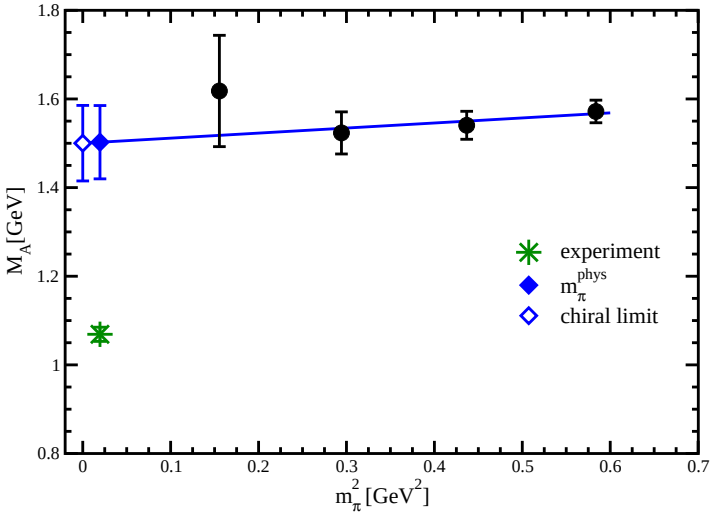

FIG. 15: Chiral extrapolation of the axial dipole mass M_A. Symbols are defined as in Fig. 8.

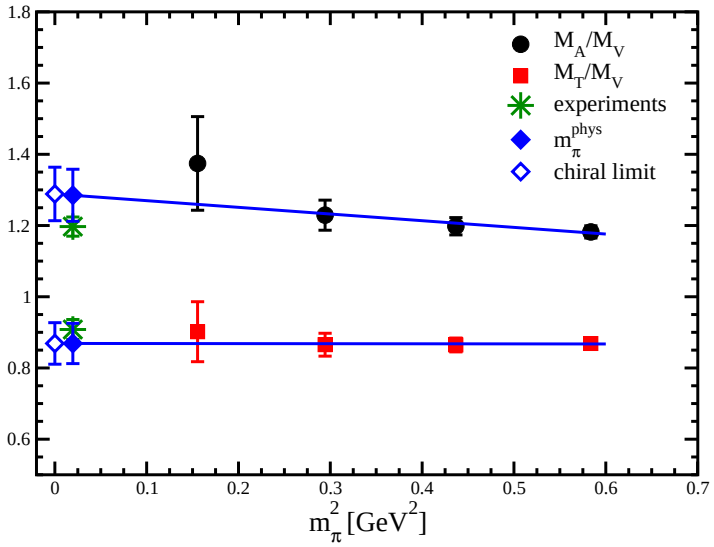

FIG. 16: Ratios, M_A/M_V and M_T/M_V as functions of squared pion mass. The extrapolated points in the chiral limit and at the physical point are represented by an open diamond and a filled diamond. The experimental values are marked with asterisk symbols.

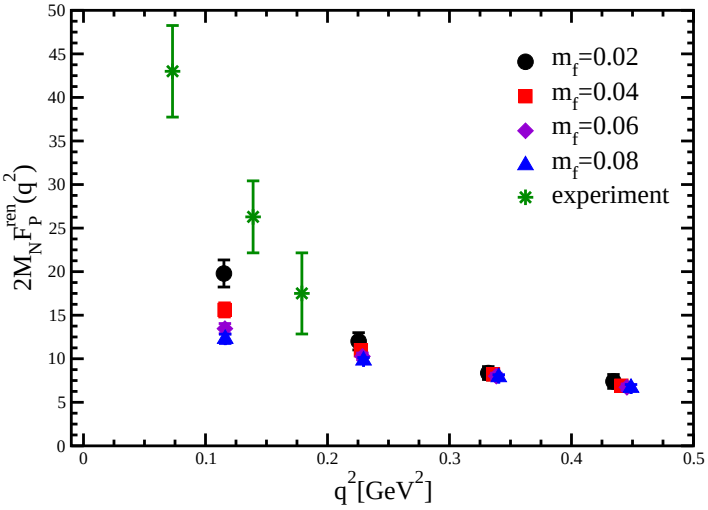

FIG. 17: The renormalized and dimensionless induced pseudo-scalar form factor $2M_N F_P^{\rm ren}(q^2)$ as a function of four-momentum squared q^2.

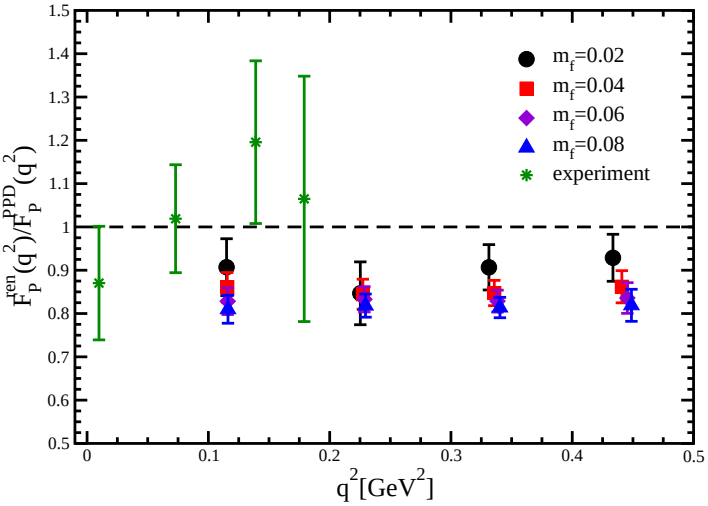

FIG. 18: The ratio of $F_P^{\rm ren}(q^2)$ and $F_P^{\rm PPD}(q^2)$ as a function of four-momentum squared q^2.

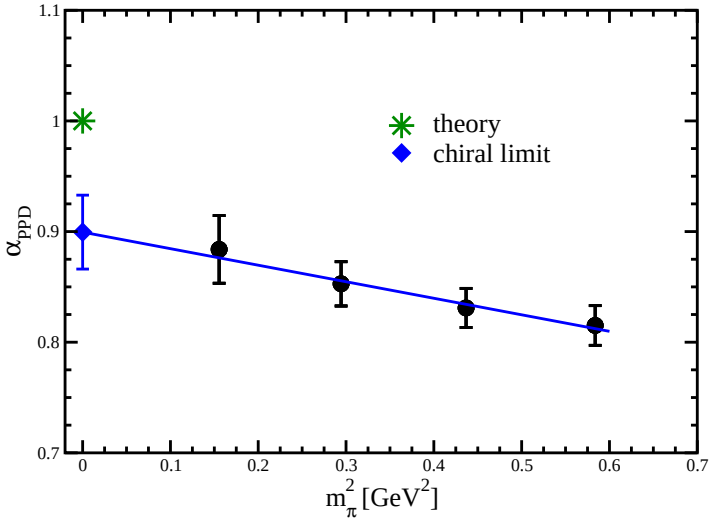

FIG. 19: The quenching factor $\alpha_{\rm PPD}$ is plotted as a function of m_π^2.

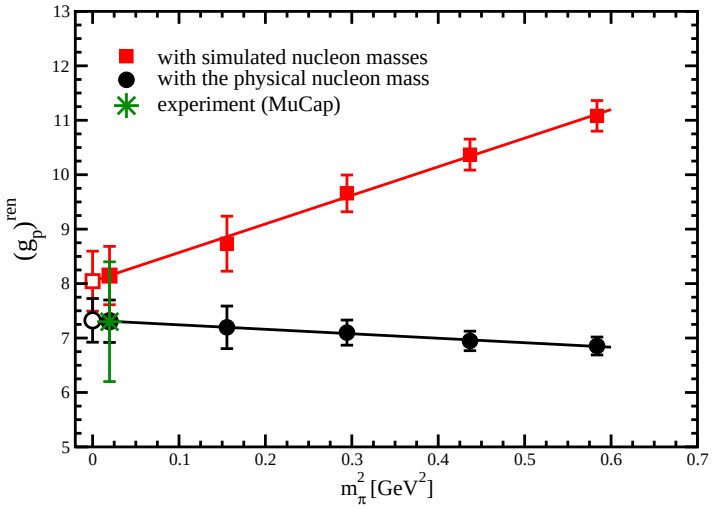

FIG. 20: The induced pseudo-scalar coupling $(g_P)^{\rm ren}$ evaluated through two determinations, where measured values (squares) and the physical value (circles) are used for the nucleon mass in Eq.(48).

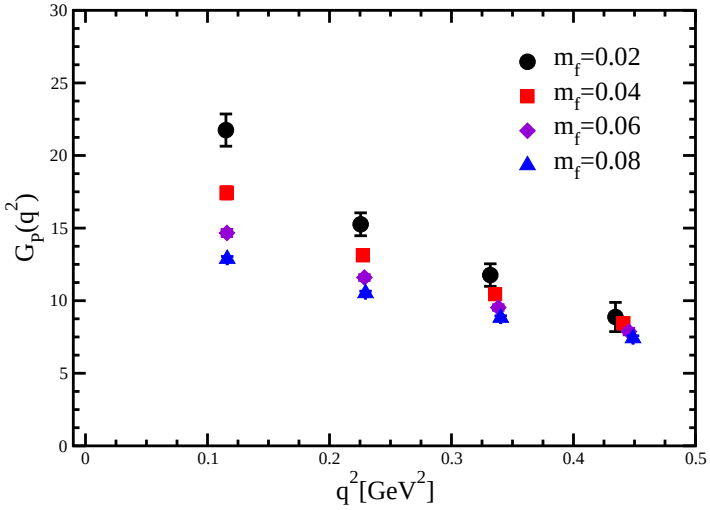

FIG. 21: The bare pseudo-scalar form factor $G_P(q^2)$ as a function of four-momentum squared q^2.

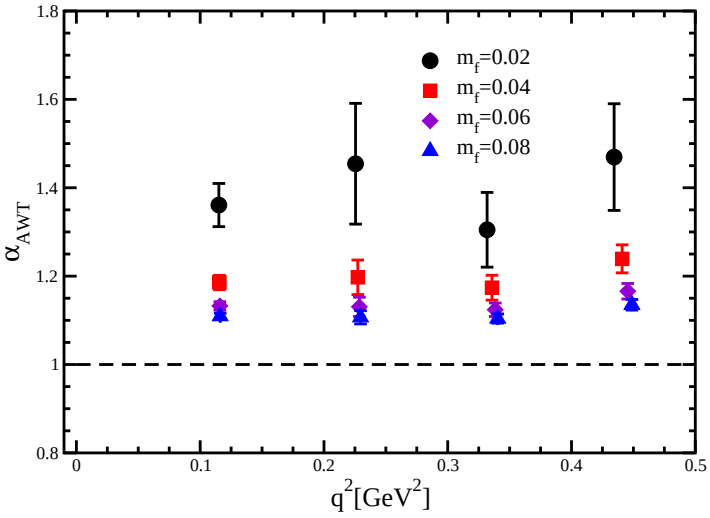

FIG. 22: The ratio $\alpha_{\rm AWT}$ defined in Eq.(59) as a function of four-momentum squared q^2.

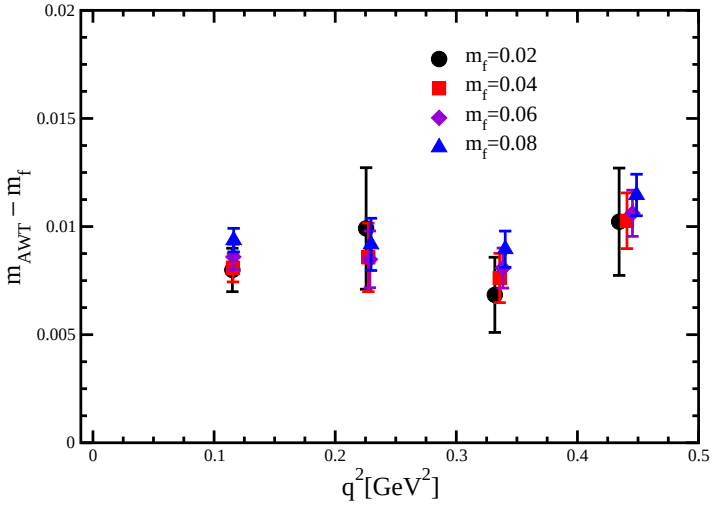

FIG. 23: The modified ratio $m_f(\alpha_{\rm AWT}-1)$, which may be expressed as $m_{\rm AWT}-m_f$, as a function of four-momentum squared q^2.

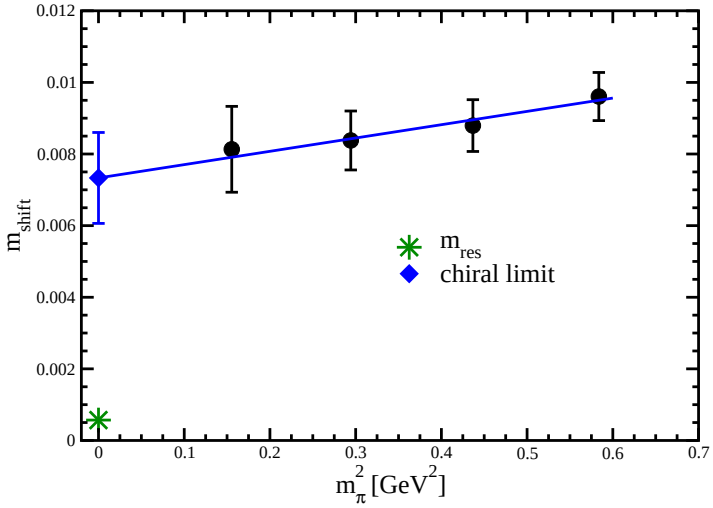

FIG. 24: The mass shift $m_{\rm shift}=m_{\rm AWT}-m_f$ as a function of pion mass squared. For a comparison, the value of $m_{\rm res}$ is included as a asterisk symbol.

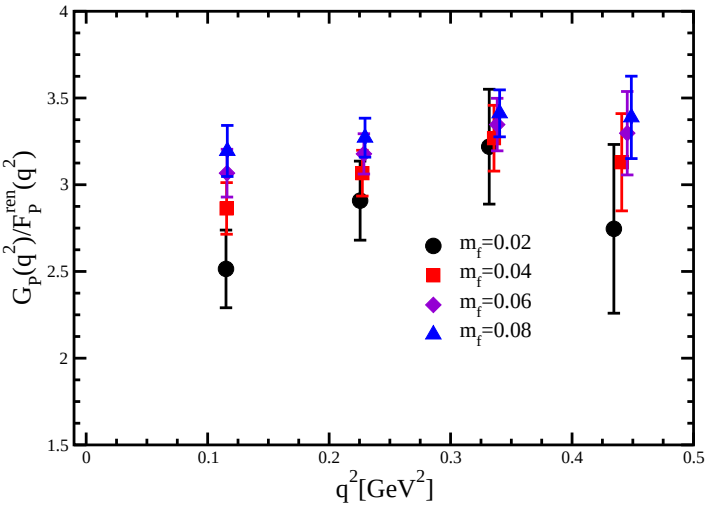

FIG. 25: The ratio of $G_P(q^2)/F_P^{\rm ren}(q^2)$ as a function of four-momentum squared q^2. A slight q^2-dependence remains against the naive expectation from the pion-pole dominance hypothesis.

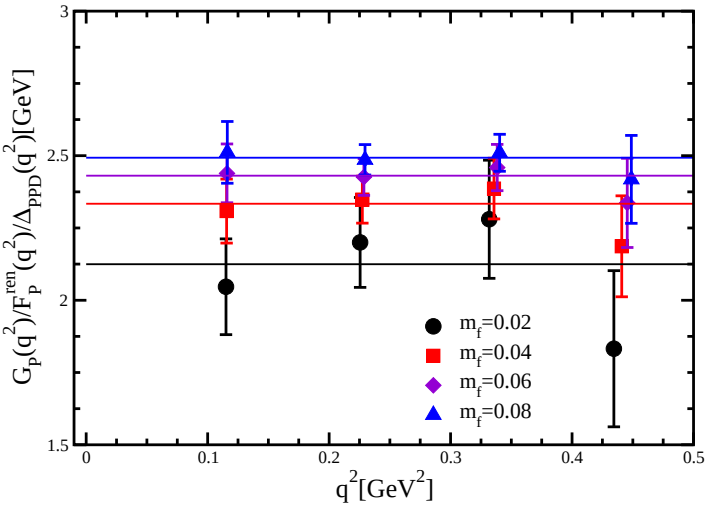

FIG. 26: The ratio of $G_P(q^2)/F_P^{\rm ren}(q^2)/\Delta_{\rm PPD}(q^2)$ as a function of four-momentum squared q^2. The residual q^2-dependence in the ratio of $G_P(q^2)/F_P^{\rm ren}(q^2)$ disappears by a multiplication of $1/\Delta_{\rm PPD}(q^2)$, which is responsible for the fact of $\alpha_{\rm PPD} \neq 1$.

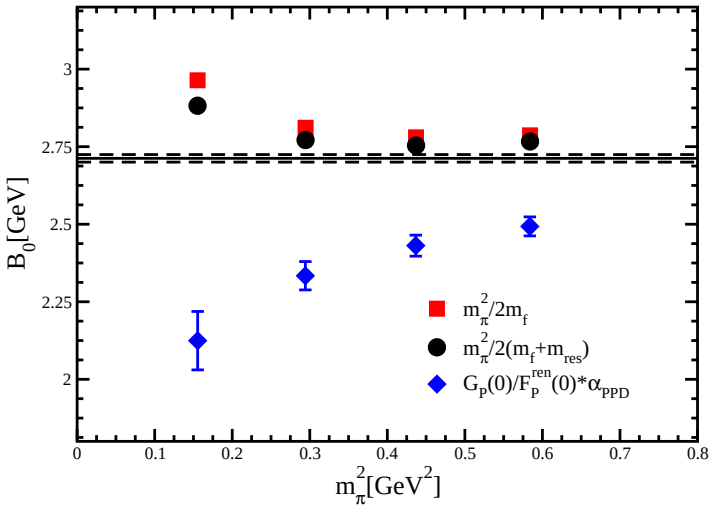

FIG. 27: The ratio of $G_P(0)/F_P^{\rm ren}(0)/\Delta_{\rm PPD}(0)$, $m_\pi^2/2m_f$, and $m_\pi^2/2(m_f+m_{\rm res})$ as functions of m_π^2.

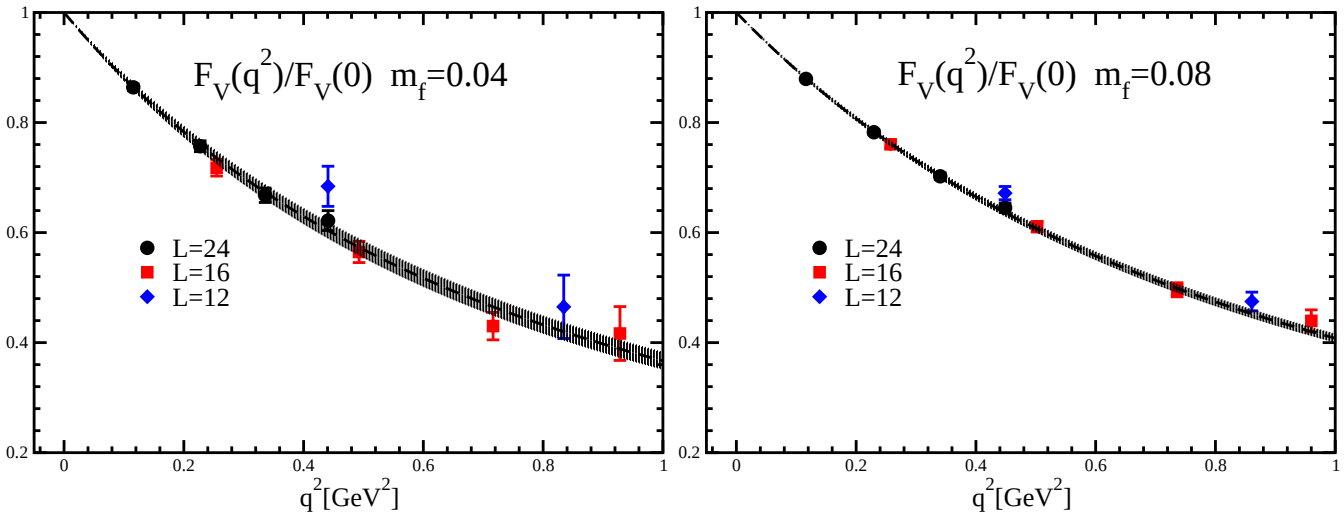

FIG. 28: The normalized vector form factor $F_V(q^2)/F_V(0)$ obtained from simulations on lattices with three different spatial sizes. The left (right) panel is for $m_f = 0.04$ ($m_f = 0.08$). Filled circles, squares and diamonds are obtained from $L = 24$, $L = 16$ and $L = 12$. The curves represent the dipole form fits on results of the largest volume ($L = 24$).

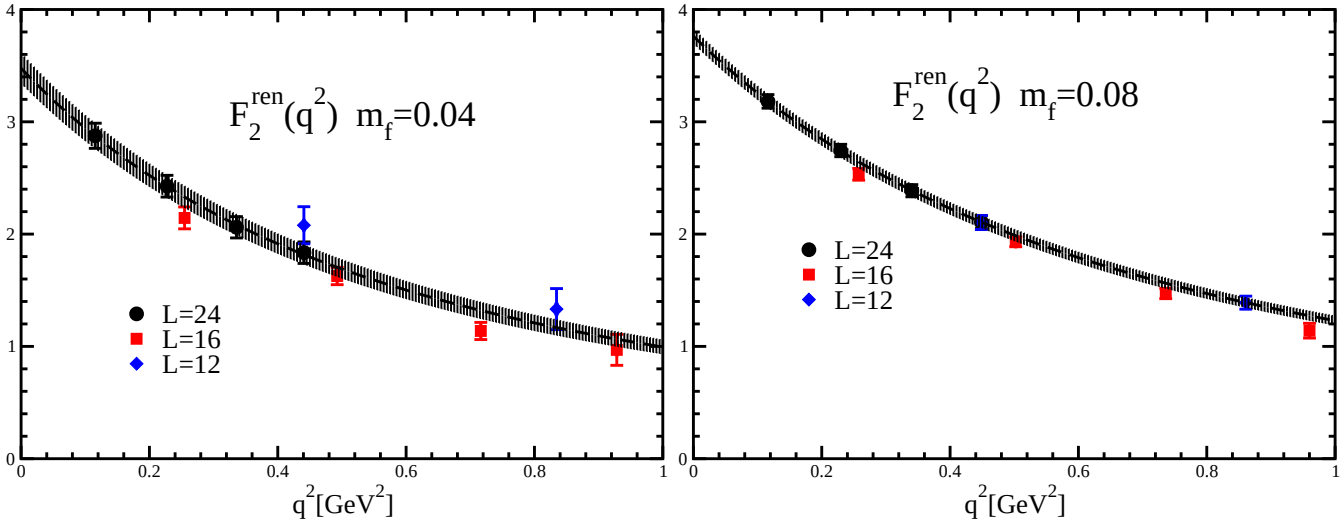

FIG. 29: The renormalized and dimensionless induced-tensor form factor $F_2^{\rm ren}(q^2) = 2M_N F_T(q^2)/F_V(0)$ obtained from simulations on lattices with three different spatial sizes. The left (right) panel is for $m_f = 0.04$ ($m_f = 0.08$). Symbols and solid curves are defined as in Figs.28.

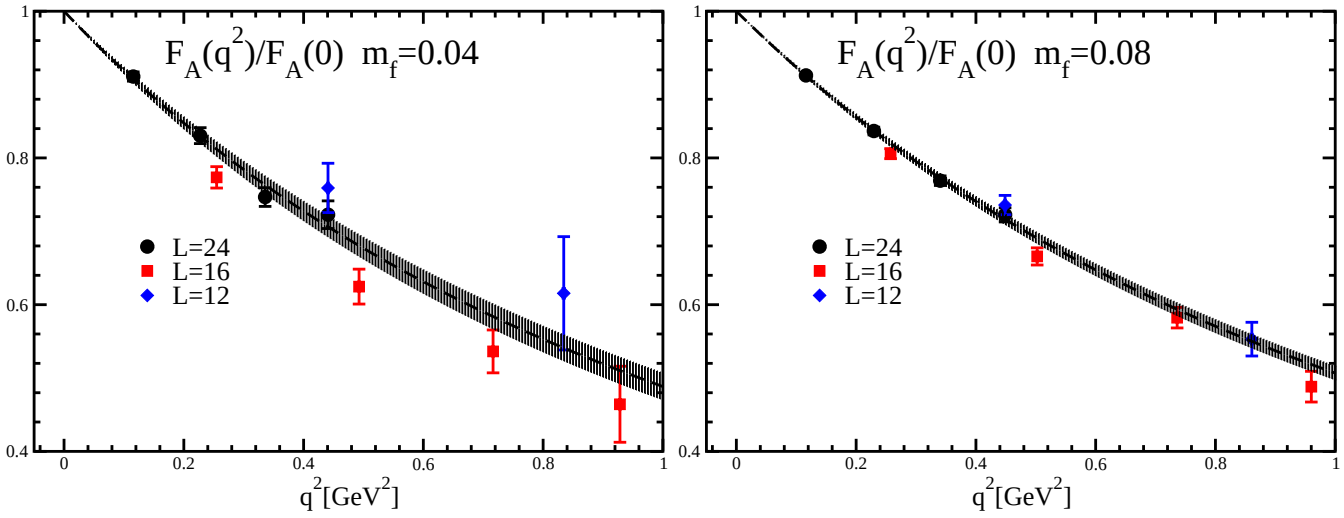

FIG. 30: The normalized axial-vector form factor $F_A(q^2)/F_A(0)$ obtained from simulations on lattices with three different spatial sizes. The left (right) panel is for $m_f = 0.04$ ($m_f = 0.08$). Symbols and solid curves are defined as in Figs.28.

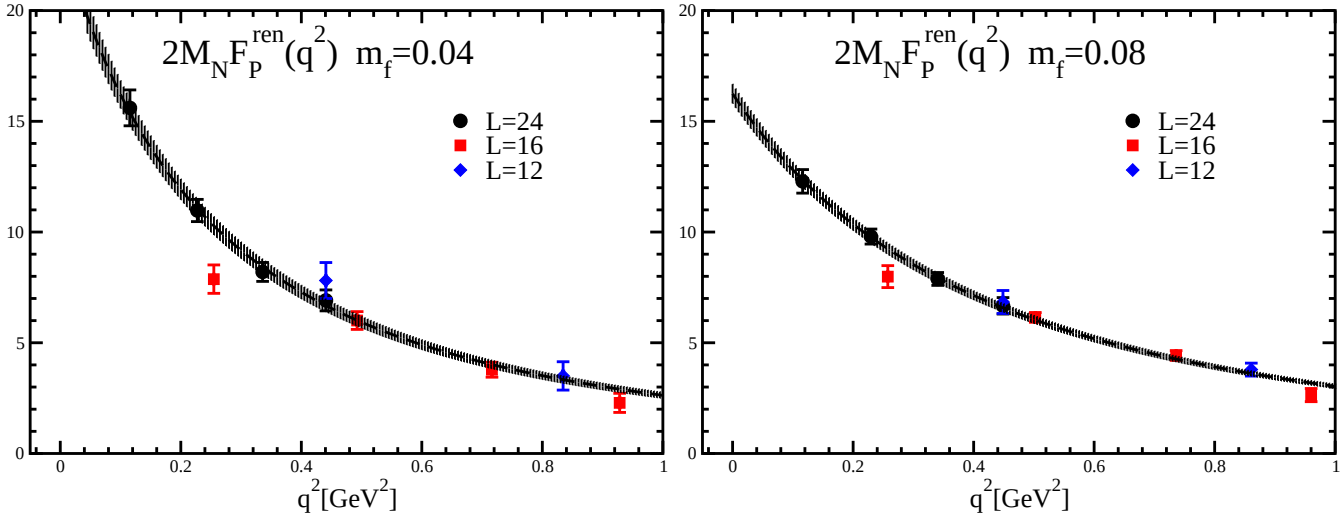

FIG. 31: The renormalized and dimensionless induced-pseudo-scalar form factor, $2M_N F_P^{\rm ren}(q^2)$ obtained from simulations on lattices with three different spatial sizes. The left (right) panel is for $m_f = 0.04$ ($m_f = 0.08$). Symbols are defined as in Figs.28. Solid curves are resulting fits with the form (47) on results of the largest volume ($L = 24$).

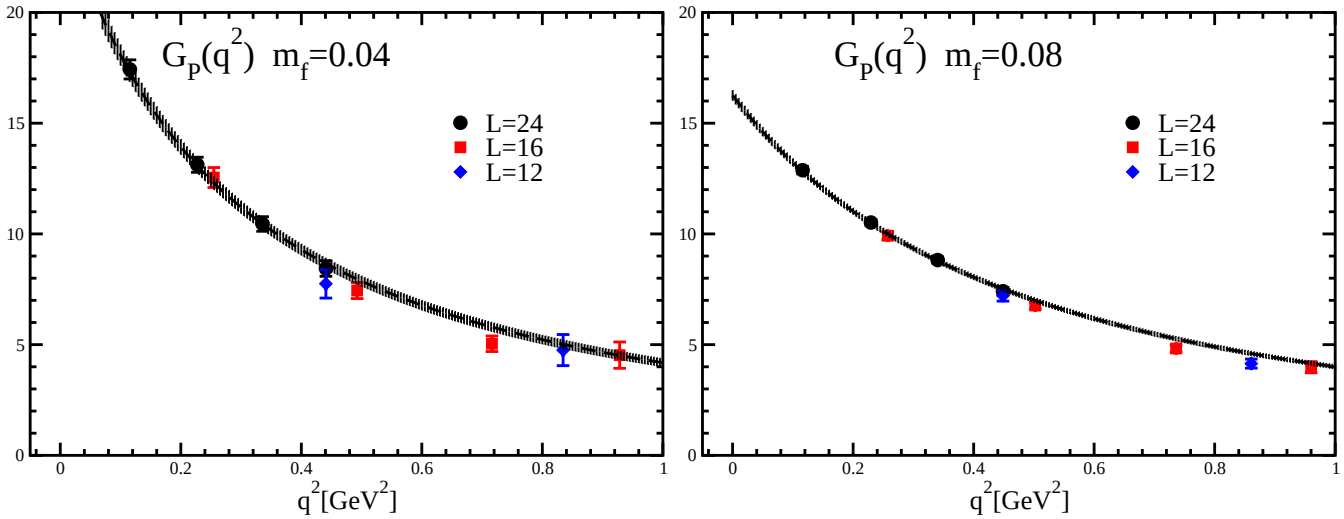

FIG. 32: The bare pseudo-scalar form factor $G_P(q^2)$ obtained from simulations on lattices with three different spatial sizes. The left (right) panel is for $m_f = 0.04$ ($m_f = 0.08$). Symbols are defined as in Figs.28. Solid curves are resulting fits with the form (63) on results of the largest volume ($L = 24$).

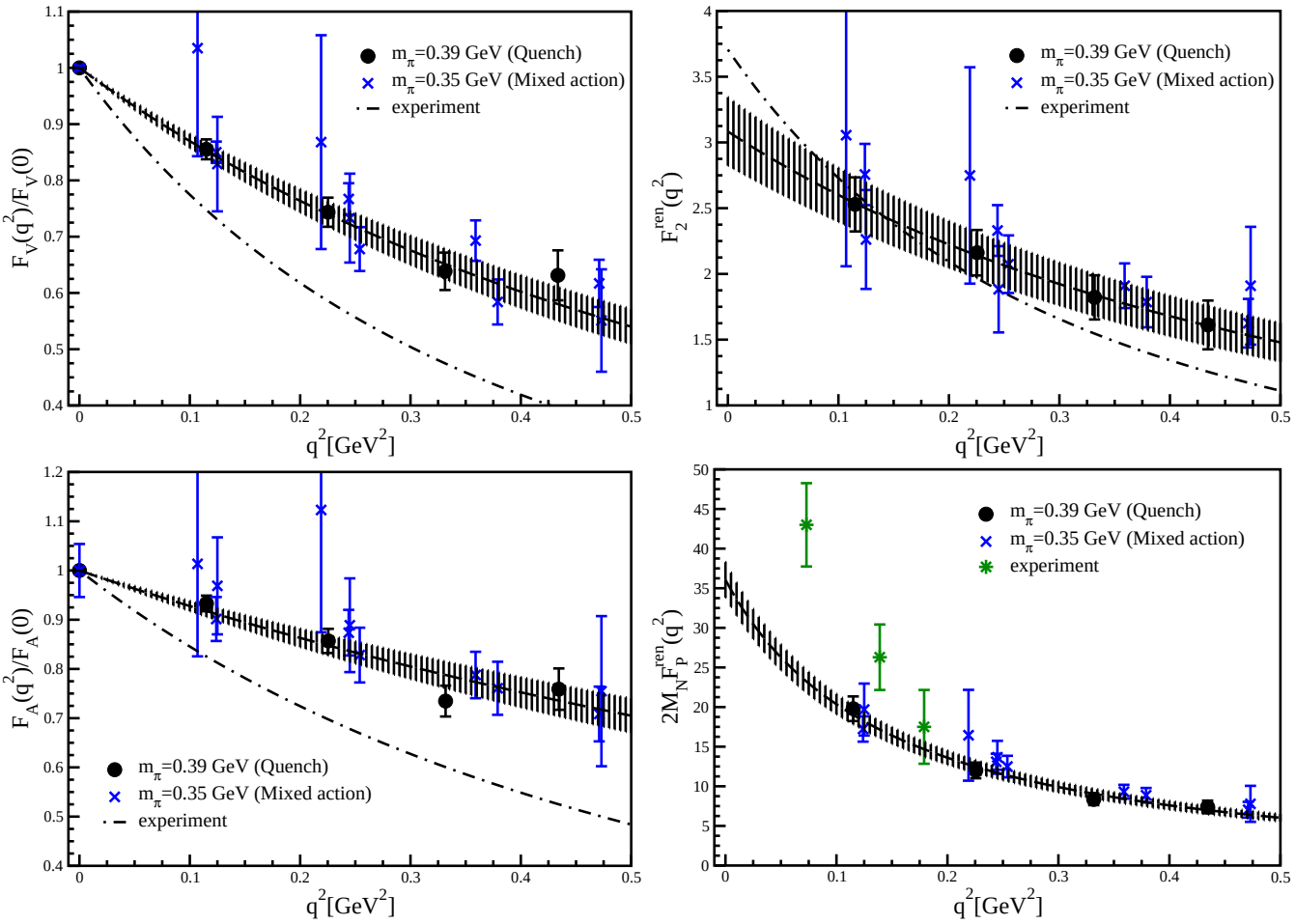

FIG. 33: Comparisons to results obtained from the LHPC mixed action results [5]. Results for all four form factors at low q^2 are consistent with each other. This suggest that unquenching effects on these form factors are still small for $m_\pi \gtrsim 0.35$ GeV.